Seasonal variation of source contributions to eddy-covariance CO_2 measurements in a mixed hardwood-conifer forest

JiHyun Kim[1,2,*], Taehee Hwang[2], Crystal L. Schaaf[3], Natascha Kljun[4], and J. William Munger[5]

[1]Department of Earth & Environment, Boston University, Boston, MA, US

[2]Department of Geography, Indiana University Bloomington, Bloomington, IN, US

[3]School for the Environment, University of Massachusetts Boston, Boston, MA, US

[4]Department of Geography, Swansea University, Swansea, UK

[5]School of Engineering and Applied Sciences and Department of Earth and Planetary Sciences, Harvard University, Cambridge, MA, US

*Corresponding author

E-mail: jk237@iu.edu

Tel: (812) 855-6303

This manuscript will be submitted to *Agricultural and Forest Meteorology*

Color reproduction of figures in print is preferred for this article.

Abstract

Net ecosystem exchange (NEE) measurements using the eddy covariance technique have been widely used for calibration and evaluation of carbon flux estimates from terrestrial ecosystem models as well as for remote sensing-based estimates across various spatial and temporal scales. Therefore, it is vital to fully understand the land surface characteristics within the area contributing to these flux measurements (i.e. source area) when upscaling plot-scale tower measurements to regional-scale ecosystem estimates, especially in heterogeneous landscapes, such as mixed forests. We estimated the source area of a flux tower at a mixed forest (Harvard Forest in US) using a footprint model, and analyzed the spatial representativeness of the source area for the vegetation characteristics (density variation and magnitude) within the surrounding 1- and 1.5-km grid cells during two decades (1993 – 2011). Semi-variogram and window size analyses using 19 years of Landsat-retrieved enhanced vegetation index (EVI) confirmed that spatial heterogeneity within the 1-km grid cell has been gradually increasing for leaf-on periods. The overall prevailing source areas lay toward the southwest, yet there were considerable variations in the extents and the directions of the source areas. The source areas generally cover a large enough area to adequately represent the vegetation density magnitude and variation during both daytime and nighttime. We show that the variation in the daytime NEE during peak growing season should be more attributed to variations in the deciduous forest contribution within the source areas rather than the vegetation density. This study highlights the importance of taking account of the land cover variation within the source areas into gap-filling and upscaling procedures.

Highlights

1. The source contribution to eddy-covariance CO_2 measurements differed between leaf development stages.
2. The variation in the daytime CO_2 measurements were accounted for by the vegetation density within the source area during the greenup and senescence stages.
3. During the maturity stage the land cover within the source area better explained the variation in the daytime CO_2 measurements.

Keywords

Eddy covariance flux measurement; Net ecosystem exchange; Spatial representativeness; Footprint model; Landsat EVI

1. Introduction

Our understanding of the interactive dynamics between climate change and terrestrial ecosystem processes (Cao and Woodward, 1998; Finzi et al., 2011; Keenan et al., 2014; Nemani et al., 2003) has been remarkably progressed through the use of tower-based eddy covariance (EC) flux measurements (Baldocchi, 2003; Baldocchi et al., 1988; Falge et al., 2002; Law et al., 2002; Schmid et al., 2000). As unique *in-situ* and semi-continuous measurements, these flux tower data have been applied to a wide range of studies, such as statistical analysis for a single site or across multiple biomes (Keenan et al., 2013; Urbanski et al., 2007), and for correlation analysis with other biophysical attributes and processes (Davidson et al., 2006).These tower data have also been used for calibration and validation of mechanical ecosystem models and remote sensing-based estimates at various spatial resolutions (e.g., the Moderate Resolution Imaging Spectrometer (MODIS) gross primary productivity (GPP) product at a 1-km resolution (Heinsch et al., 2006; Schwalm et al., 2010; Verma et al., 2015). The number of flux towers in the FLUXNET network (http://fluxnet.ornl.gov/) has increased rapidly, including about 846 sites as of November 2016. Mixed forests are some of the most common land covers in which flux towers have been set up (https://fluxnet.ornl.gov/site_list/IGBPLU/5). Several of the flux towers with the longest records, therefore the towers most frequently used in studies, are located in mixed forests such as Harvard Forest, MA, US (FLUXNET Site ID: US-Ha1, since 1991), Howland Forest, ME, US (US-Ho1,2,3, since 1995,1999,2001), Morgan-Monroe State Forest, IN, US (US-MMS, since 1998), ON-Borden Mixed wood, Ontario, Canada (CA-Cbo, since 1995), Brasschaat, Belgium (BE-Bra, since 1996), and more.

Multiple factors have to be considered to determine whether the upwind land surface measured by a flux tower ("*source area*") adequately describes the characteristics of the

surrounding ecosystem ("*spatial representativeness*"; Román et al., 2009; Schmid, 1997). This is especially critical in mixed forests, where temporally varying wind direction and atmospheric stability can change the source weight distribution of fluxes measured at a tower considerably over the heterogeneous land covers, resulting in a large degree of variations in the source area characteristics and therefore in the measured flux (Wehr and Saleska, 2015). This inevitable source area variability has long been recognized as one of the major uncertainties in flux measurements (Baldocchi, 2003). To understand and reduce this uncertainty, a number of studies have focused on developing a source weight function ("*footprint*"; Hsieh et al., 2000; Kljun et al., 2002, 2004; Kormann and Meixner, 2001; Schmid, 1994; van Ulden, 1978) and applying these footprint models for the uncertainty analysis of flux measurements and also for ground-biometric sampling schemes (Amiro, 1998; Chasmer et al., 2011; Griebel et al., 2016; Novick et al., 2014; Oishi et al., 2008; Stoy et al., 2006; Xu et al., 2017). There are also ongoing efforts to standardize the source area estimation at the network levels (Menzer et al., 2015, 2014). However, as of yet, most studies of mixed forests have not fully considered the temporal variations in source areas, but instead have only approximated a fixed area (Turner et al., 2003; Verma et al., 2015) or simply rejected some flux data solely based on wind direction (Daley et al., 2007; Phillips et al., 2010). Such wind-direction based filtering schemes sometimes leave only 25% of the total data deemed as appropriate for further analysis (Hadley & Schedlbauer, 2002; Stoy et al., 2006), yet still leaves questions about the representativeness of the flux data for large-scale applications.

Furthermore, even those studies that assessed the spatial representativeness of flux measurements for the surrounding landscape using footprint models have usually only performed this assessment for a limited time period, such as for a single season or for only a few years,

mainly due to the high computational costs (Chen et al., 2012; Göckede et al., 2008; Kim et al., 2006; Schmid and Lloyd, 1999). In a mixed forest, however, the spatial representativeness of source areas may experience significant seasonal variations, depending on vegetation types and their spatial distributions around the tower. For example, the phenological stage of deciduous trees (greenup, maturity, senescence, and dormancy onsets) can be a primary factor that transforms the entire surrounding landscape and drives the seasonal cycle of flux measurements. Román et al. (2009) showed that the representativeness of tower-based albedo measurements (note: a tower albedometer has a fixed viewing angle) for the evaluation of moderate resolution satellite-derived albedo products is largely dependent on the timing of greenup of deciduous trees, the distribution of conifer trees within the source area, and gridded resolutions of the satellite products (~1-km and 1.5-km). The intrinsic physiological differences among vegetation functional types also contribute to the spatial variations in biophysical attributes over the landscape. Tian et al. (2002) described that 76% of total variance in leaf area index (LAI) within a 15 × 13 km area in a mixed forest is mostly governed by the spatial variation of vegetation functional types. There are also additional factors driving interannual and long-term changes in spatial landscape characteristics of mixed forests, such as the different sensitivities to interannual climate variability (Welp et al., 2007) and changes in vegetation types and distributions due to ongoing climate change (Battles et al., 2007). Therefore, it is critical to understand long-term representativeness of source areas when interpreting flux measurements in mixed forests and when using these measurements to evaluate ecosystem models and remote sensing-based models across different temporal and spatial scales.

In this study, first we calculate hourly source weights for a flux tower in a mixed forest for 19 years (1993-2011). Based on these source weight estimates, we then examine the

representativeness of the source area for the surrounding vegetation characteristics (density magnitude and variation) at moderate-spatial resolutions (1-km and 1.5-km) during daytime and nighttime, separately, for each phenological stage. Finally, we investigate how much of the variation in the measured flux can be attributed to vegetation density and land cover based on their footprint-weighted contributions.

2. Materials and Methods

2.1. Study site

The Environmental Measurement Site tower (42.537755 °N, 72.171478 °W; US-Ha1) is located in the Harvard Forest Long Term Ecological Research (LTER) site in Petersham, Massachusetts. The topography in this area is relatively moderate, with elevation ranging from 320 to 380 meters above sea level (Fig. 1a). The forest has a cool and moist temperate climate with annual mean temperature of about 8.5 °C (20 °C in July and -7 °C in January) and annual total precipitation of approximately 1100 mm, with winds primarily from southwest and northwest (http://harvardforest.fas.harvard.edu/research/HF-tract). The forested landscape is dominated by several tree species, including northern red oak (*Quercus rubra*), red maple (*Acer rubrum*), eastern hemlock (*Tsuga canadensis*), white pine (*Pinus strobus*), and black birch (*Betula lenta*) (Urbanski et al., 2007). Mean ages of northern red oak and eastern hemlock are about 97 and 145 years, respectively (Belmecheri et al., 2014). Canopy height is at about 20-24 meters (Goulden et al., 1996; Wang et al., 2011). Basal area is about 33.5 m^2 ha^{-1} (Munger and Wofsy, 1999a). Deciduous trees occupy the southwestern area from the tower with scattered patches of coniferous trees (Fig. 1b). In mid-September of 1999, beaver activity caused a flood on the northwest side of the tower, developing a small woody wetland (Savage et al., 2001; Urbanski et al., 2007). Additional beaver activity temporarily flooded an area along the Bigelow brook on the southeast side of the tower in recent years. This forest has been experiencing a hemlock woolly adelgid infestation since late 2000s (Orwig et al., 2008), but significant hemlock mortality was not yet been observed close to the tower over the study period (until 2011; Kim et al., 2017).

151 The tower measurements, which began in Oct 1991, provide the longest continuous set of
152 flux measurements in the US (Baldocchi et al., 1988; Goulden et al., 1996; Urbanski et al.,
153 2007). Ground transects were established in 1993 along the prevailing wind directions, southwest
154 and northwest (220-254 and 291-325 compass degrees). Since 1995, biometric and abiotic data
155 has been collected along these transects 20-30 times a year, which include soil samples (water
156 content, temperature and respiration), biomass measurements (leaf area index, litterfall and
157 woody debris), and below-canopy microclimate observations (air temperature and solar
158 radiation). Datasets are publicly available on the Harvard Forest LTER, AmeriFlux and
159 FLUXNET websites (http://harvardforest.fas.harvard.edu; http://ameriflux.lbl.gov; Munger and
160 Wofsy, 1999a, 1999b).
161

162 *2.2. Data overview*

163 We used the hourly quality-checked NEE data (g C m^{-2} s^{-1}) of the FLUXNET2015
164 dataset (http://fluxnet.fluxdata.org/data/fluxnet2015-dataset/; data quality assessment processes
165 are described in Pastorello et al. (2014)). Micrometeorological and energy flux data such as
166 friction velocity (u^*), wind direction (α), the standard deviations and covariances of wind
167 components (σ_u, σ_v, σ_w, $\overline{u'v'}$, $\overline{u'w'}$), air temperature (T_{air}), photosynthetically active radiation
168 (PAR), vapor pressure deficit (VPD), and sensible heat flux (H), were acquired at the above-
169 canopy 29 m point of the tower as was the NEE data (Munger and Wofsy, 1999b; additional data
170 upon request: tower PI J. William Munger). Only directly measured NEE data was used to avoid
171 any uncertainty or bias in gap-filling procedures, and the u^* threshold was set to 20 cm s^{-1}
172 (Urbanski et al., 2007).

173 At the study site, visual observations of the percentage of leaf size (from April through
174 June) and the percentage of colored leaves on a tree (from September through November) have
175 been performed at every 3-7 days since 1990 (O'Keefe, 2000). We used the observation data of
176 the two dominant deciduous species (northern red oak and red maple) from 1993 to 2011 to
177 determine the phenological stages of the deciduous broadleaf forest (DBF). A piecewise logistic
178 function (Eq. (1) and Fig. 2) was fitted to leaf size and coloration data, respectively, for each
179 year (Fig. S2). The dates when the curvature of the fitted function has the greatest changes were
180 defined as four phenological transitional dates: greenup, maturity, senescence, and dormancy
181 onsets (Hwang et al., 2011; Zhang et al., 2003).

182 $$I(t) = \frac{1}{1+e^{a+t\cdot b}} \quad (1)$$

183 where *I(t)* is index from leaf data, *t* is the day of year. The fitting coefficients (*a* and *b*) were
184 estimated using a nonlinear regression (*nlinfit*, Matlab R2013a, MathWorks Inc., Natick, MA).
185 The three phenological stages (i.e. greenup, maturity, and senescence) are the periods between
186 the phenological transitional dates (Fig. 2).

187 We collected all available Landsat-5 Thematic Mapper (TM) and Landsat-7 Enhanced
188 Thematic Mapper Plus (ETM+) scenes from 1993 to 2011 (http://earthexplorer.usgs.gov/;
189 Landsat-7 during 1999-2003). Landsat scenes have high spatial- and moderate temporal-
190 resolutions (30 m and 16 day overpass cycle), and they cover the entire study period, which
191 facilitates efficient and consistent assessments of the landscape heterogeneity at the study site.
192 We retrieved surface reflectance data on only cloud-free days using the Landsat Ecosystem
193 Disturbance Adaptive Processing System (LEDAPS; Masek *et al.*, 2006). In this study, we used
194 the enhanced vegetation index (EVI; Eq. (2)) as an indicator of vegetation density (e.g. LAI)

because EVI is more sensitive to LAI in a closed canopy forest than other vegetation indices (Gao, 2000; Huete et al., 2002).

$$EVI = G\frac{\rho_{nir} - \rho_{red}}{\rho_{nir} + C_1 \cdot \rho_{red} - C_2 \cdot \rho_{blue} + L} \quad (2)$$

where ρ is the surface reflectance in near-infrared, red, and blue bands (ρ_{nir}, ρ_{red}, and ρ_{blue}), C_1 and C_2 are the aerosol resistance coefficients, G is gain factor, and L is the canopy background adjustment. The coefficients are set as follows: L=1, C_1=6, C_2=7.5, and G=2.5 (Huete et al., 2002).

The land cover in this study is based on three National Land Cover Dataset products at five-year intervals (NLCD 2001/2006/2011; http://www.mrlc.gov/). The NLCD 1992 was not included in this study because the land cover definitions in the NLCD 1992 are different from those defined in the others (Trotter et al., 2013). These NLCD products were derived from Landsat imagery, therefore having a spatial resolution of 30 m..

2.3. Footprint model and flux source attributes

We calculated the hourly source weights (φ) for the directly-measured and quality-checked hourly NEE data from 1993 to 2011 using the Flux Footprint Prediction (FFP) model (Kljun et al., 2015; http://footprint.kljun.net). For the FFP model, the sensor height parameter (z_m) was set to the instrument height minus the zero-plane displacement height (d = 2/3 times the canopy height; Stull, 1988). The sonic anemometer is mounted at 29 m on the tower, and the canopy height was set to 21 m in this study. Manual observations in 1992 when the tower was installed (Goulden et al., 1996) and airborne LiDAR measurements in 2003 (Fig. S1; Park et al., 2014; Wang et al., 2011) show no significant differences outside their respective uncertainty and

spatial variability. Further input parameters, such the standard deviation of lateral velocity fluctuations (σ_v), the friction velocity (u_*), and the wind direction were all directly derived from the EC data. The surface roughness length (z_0) was set to 1.6 m for both deciduous and coniferous canopies at the study site (Hadley and Schedlbauer, 2002; Wu et al., 2015). The planetary boundary layer (h) was calculated depending on the atmospheric stability, such as stable (Obukhov length, L > 0), neutral (L → ∞), and convective (L > 0) conditions (Kljun et al., 2015). It should be noted that the FFP model assumes the upwind domain is spatially homogeneous, a condition that is complied with at the study site where the topography is moderate (elevation variation less than 60 m) and the canopy height distribution is mostly even (Fig. S1; standard deviation (SD) of 2.6 m within the 500-m grid cell; Wang et al., 2011).

In this study, we limited the extent of an source area at the 80% source weight (φ_{80}) as the uncertainty of any footprint model increases for larger extents (Kljun et al., 2015). We then calculated the geometric mean of the along-wind distance from the tower and the crosswind distance at the peak location.

We focused on two flux source attributes: vegetation density and land cover type. We calculated the 1-km grid cell mean EVI ($\overline{EVI}_{1km}$) and footprint-weighted EVI ($EVI_{\varphi 80}$ in Eq. (3); Kim et al., 2006).

$$EVI_{\varphi 80} = \sum_{i=1}^{N_{\varphi 80}} \varphi_{80,i} EVI_i \quad (3)$$

where i designates one pixel, and $\varphi_{80,i}$ and EVI_i are the source weight (φ_{80}) and the EVI value at i-pixel. $N_{\varphi 80}$ refers the total number of pixels within the source area. The relative contribution of each land cover to flux measurements, i.e., the footprint-weighted proportion of each land

cover ($P_{\varphi 80}$; Eq. (4)), was calculated by summing and normalizing the source weights of the respective land cover (Chen et al., 2013).

$$P_{\varphi 80,k} = \frac{\sum_{i=1}^{N_k} \varphi_{80,i}}{\sum_{i=1}^{N\varphi 80} \varphi_{80,i}} \times 100 \quad (4)$$

where N_k refers to the total number of pixels for each land cover (k) within the source area. Due to the limited availability of the NLCD for the early 1990s, we did not include the first 6 years of the study period (1993-1998), and partitioned the remaining study periods to situate each NLCD at the center year: NLCD 2001 for the 5 years from 1999 to 2003, NLCD 2006 from 2004 to 2008, and NLCD 2011 for the other 3 years (2009-2011).

2.4. Quantification of spatial heterogeneity

The semi-variogram model has been recognized as one of the most efficient tools to describe spatial heterogeneity and autocorrelation in sample measurements (Carroll and Cressie, 1996; Curran, 1988; Davis, 1986; Woodcock et al., 1988a), ranging from abiotic phenomena (e.g. temperature and precipitation; Haylock et al. 2008) to biophysical attributes (e.g. surface vegetation albedo; Román et al. 2009). The semi-variance is defined as the average of the half variances of *N(h)* pairs of observations at an interval distance (lag distance) of *h* (Curran, 1988). The semi-variance estimator ($\bar{\gamma}_{EVI}(h)$; Eq. (5)) here was calculated as half the average-squared-difference between EVI values at a pair of pixels separated by a distance *h*.

$$\bar{\gamma}_{EVI}(h) = \frac{\sum_i^{N(h)} \gamma_i(h)}{N(h)} = \frac{\sum_i^{N(h)} (Z_{xi} - Z_{xi+h})^2}{2N(h)} \quad (5)$$

where Z_{xi} is the EVI value at a pixel (x_i), and Z_{xi+h} is the EVI value at a pixel (x_{i+h}) within a lag distance *h*, therefore a multiple of 30 m in this study which is the nominal resolution of Landsat scenes. The maximum lag distance for a 1-km grid cell is 690 m, half of the length of the diagonal of the 1-km boundary. The isotropic spherical variogram model in Eq. (6) (Matheron 1963) was fitted to the semi-variance estimators to obtain the variogram parameters: *nugget effect* (c_0), *sill* (c), and *range* (a) in Fig. 1d.

$$\gamma_{SPH}(h) = \begin{cases} c_0 + c\left(1.5\left(\frac{h}{a}\right) - 0.5\left(\frac{h}{a}\right)^3\right), & 0 \le h < a \\ c_0 + c, & h \ge a \end{cases} \quad (6)$$

The *nugget effect* is an estimation of the variance at a lag distance of zero, indicating microscale variability within the smallest sampling distance, uncertainty in the measurements, or combination of both factors (Noréus et al., 1997). The *sill* represents a horizontal asymptote value of the variogram model, reflecting absolute magnitude of heterogeneity within the study grid cell (1-km and 1.5-km in this study). The variogram reaches the *sill* at the lag distance, *range*, beyond which there is no further spatial covariance between biophysical properties. We quantified the spatial variation in the vegetation density at moderate resolutions (1 and 1.5-km) with the semi-variogram model using the Landsat-retrieved EVI from 1993 to 2011 (Román et al., 2009; Susaki et al., 2007). Examples of the EVI maps retrieved from the Landsat scenes of the 1-km and 1.5-km grid cells centered at the tower during greenup, maturity, and senescence stages are shown in Fig. 1c.

While a semi-variogram analysis provides information about the spatial variation of the entire study grid cell, spatial heterogeneity surrounding the tower can be assessed with a window size analysis (Kim et al., 2006). The vegetation density index (EVI in this study) within a window centered at the tower was averaged ($\overline{EVI}$) for increasing size of the window (to a square

window). The window-averaged EVI difference from the 1-km grid cell mean EVI (ΔEVI_i; Eq. (7)) was calculated as the window width increased

$$\Delta EVI_i = \overline{EVI}_i - \overline{EVI}_{1km} \quad (7)$$

while $\overline{EVI}_{1km}$ refers to the 1-km grid cell mean EVI, and the size of window (i) increases by multiples of 30 m, the nominal resolution of Landsat scenes: i = 30, 90, …, 990 m (approximate width of $\overline{EVI}_{1km}$), …, 1500 m.

2.5. Significant factors of flux variation

We examined how much variation in the hourly NEE could be accounted for by the flux source attributes (i.e. vegetation density and land cover type) during each phenological stage. To minimize the confounding effects of the weather and source weight distributions, the hourly NEE data was classified into a series of classes depending on its meteorological condition (Wu et al., 2013). Each meteorological class is a combination of temperature (equal intervals of 10 °C), PAR (50 μmol m^{-2} s^{-1}), and VPD (100 pascal) classes, resulting in 8405 in total.

We applied an ordinary least squares (OLS) regression between NEE and the vegetation density measure ($EVI_{\varphi 80}$) for the meteorological classes when at least 10 observations of both EVI and NEE on the same day with EVI are available (Wu et al., 2013). We also examined the correlation between NEE and $\overline{EVI}_{1km}$ for a meteorological condition when each of temperature, VPD, and PAR was beyond the 75th percentile value of its cumulative distribution function (Fig. S4). We then examined the correlation of the land cover type with a multiple linear regression between NEE and the footprint-weighted land cover proportions ($P_{\varphi 80}$) for each meteorological

class. We assumed that the measured NEE were only contributed from the vegetated land covers, therefore the intercept was forced to zero (Hutjes et al., 2010).

$$NEE = \sum_{k=1}^{n} f_k P_{\varphi 80,k} \quad (8)$$

where n is the number of land covers (n = 4) and f_k is the coefficient for land cover k (deciduous broadleaf forest (DBF), evergreen needleleaf forest (ENF), mixed forest (MF), and woody wetland). A negative f_k indicates a carbon uptake rate per unit land cover proportion (g C m^{-2} s^{-1} $\%^{-1}$) as a negative NEE means an uptake from the atmosphere in this study. This analysis was carried out for 13 years (1999-2011) due to the limited availability of the NLCD products. The adjusted coefficient of determination (R^2_{adj}) of the OLS regression (against $EVI_{\varphi 80}$) and the R^2_{adj} of the multiple linear regression (against $P_{\varphi 80}$) was then compared separately for daytime (PAR > 50 µmol m^{-2} s^{-1}) and nighttime during each phenological stage.

3. Results

3.1. Phenological onset timings and stages

The phenological transitional timings have varied every year (Fig. S3), and the greenup stage was from May 10 to June 5, the maturity stage (peak growing season) from June 5 to September 17, and the senescence stage from September 17 to October 19 on average from 1993 to 2011. Growing season was defined from the greenup onset to the dormancy onset, therefore from May 10 to October 19 on average.

3.2. Footprint extent and distribution variation

At the tower, the prevailing wind directions over the study period were mostly southwest and northwest during both the daytime and nighttime (Fig. S5a; Davidson et al., 2006; Urbanski et al., 2007), but there were variations in the wind speed frequency distribution between the phenological stages (Fig. S5b). Strong northwesterly and westerly winds are noticeable during the greenup and senescence stages (Fig. S5b). Prevailing wind direction and frequency are of high impact to the source weight distribution, therefore the dominant orientation of source areas were mostly toward the southwest (source weight peak locations at 212-236°; Fig. S6) while there were more variations during the greenup and senescence stages. Furthermore, there was a noticeable difference in the source area sizes between the daytime and nighttime (Fig. 3) as source areas had larger extent with larger variation due to the stable atmospheric condition during nighttime (Fig. S6). The geometric mean of along-wind and crosswind distances was mostly different between the daytime and nighttime, while rather similar across phenological stages (163.5-190.6 with standard deviation (SD) of 55.8-70.4 m during the daytime, and 298.9-

221.8 with SD of 128.8-159.6 m during the nighttime). The distance between the tower and source weight peak location was also smaller and less variable during the daytime than during the nighttime, 39.4±3.4 and 58.3±30.4 m, respectively (Fig. S6).

The 1-km grid cell around the tower from the NLCD 2001 primarily consisted of DBF (Fig. S8). The transition from the NLCD 2001 to the NLCD 2006 shows that there was a slight expansion of the wetland on the northwest side of the tower. There were considerable changes from the NLCD 2006 to the NLCD 2011 due to flooding and draining of the wetlands on the northwest and southeast sides of the tower. The 1-km grid cell consisted of 47.5% of DBF, 22.1% of ENF, 15.0% of mixed forest, and 10.9% of woody wetland in the NLCD 2001, while it consisted of 47.7% of DBF, 16.2% of ENF, 14.8% of mixed forest, and 15.3% of woody wetland in the NLCD 2011. The footprint-weighted land cover proportions ($P_{\varphi 80}$; Eq. (4)) were quite different for the daytime and nighttime, relatively similar across the phenological stages (Fig. 4), due to the combined effect of the heterogeneous landscape and the variations in source areas. During the daytime, DBF is the most dominant land cover contributing about 78.3% of measured fluxes on average (SD of 19.0%), which is about 30% higher than the nominal proportion of DBF within the 1-km grid cell in the NLCD. During the nighttime, the $P_{\varphi 80}$ of DBF was slightly lower and more variable than during the daytime, at about 71.3% on average (SD of 25.1%). ENF contributed 14.5% and 19.0% during the daytime and nighttime, respectively (SD of 15.9-19.1%). The $P_{\varphi 80}$ of other covers (mixed forest, woody wetland, and open space area) were less than 5%, respectively (Fig. 4).

354 *3.3. Spatial heterogeneity of the study site*

355 The *nugget effect* values (Fig. 5a) (indicators of measurement errors or microstructures
356 within the grid cells) were primarily driven by canopy closure (i.e. phenological stage), rather
357 than long-term landscape changes. The *nugget effect* values of the 1-km grid cell were higher
358 than 0.0005 before the entire growing seasons started, and the values substantially declined by
359 the beginning of the greenup stages. As the forest canopy at the sub-pixel scale was almost
360 completely closed during the entire growing seasons, there were almost no sub-pixel scale
361 variations (*nugget effect* values ~ 0), although the values started to increase at the end of the
362 senescence stages as open canopy gaps started to contribute to increased microstructures over the
363 study site. The non-vegetated area and woody wetlands at the northeast corner of the 1.5-km grid
364 cell (Fig. 1b) caused a high level of *nugget effect* values during the maturity and senescence
365 stages (Woodcock et al., 1988b).

366 There were also seasonal and long-term changes in the *sill* values (the overall changes in
367 the spatial heterogeneity within the study grid cells) (Fig. 5b and Fig. S7a). In the early 1990s,
368 the *sill* values of 1-km grid cell were low and nearly constant (around 0.002) throughout the
369 entire growing seasons. Because of the wetland on the northwest side of the tower (Fig. S7b), the
370 spatial variations started to increase during the maturity stage of 2001, although these variations
371 consistently returned to a low level by the end of each senescence stage. The other wetland on
372 the southeast side of the tower has contributed to the gradual increase in spatial variations within
373 the 1-km grid cell during the maturity stages for the last few years (Fig. 5b and Fig. S7a). The
374 flooding and draining of those two wetlands did not have any significant impact on the spatial
375 variation of the 1.5-km grid cell which was already heterogeneous before the wetland expansion
376 (Fig. 5b).

The *range* values (the distance limit within which the surface variations are auto-correlated) within the 1-km grid cell were mostly constant during the entire growing seasons (Fig. 5c). Most of the *range* values (280 m, 265 m, and 250 m on average during the greenup, maturity, and senescence stages, respectively) were within one standard deviation of the geometric mean of along-wind and crosswind distances during both the daytime and nighttime. The *range* values of the 1.5-km grid cell were higher than those of the 1-km grid cell due to the non-vegetated area at the northeastern corner (Fig. 1b).

ΔEVI, the difference between the window-averaged EVI and 1-km grid cell averaged EVI (i.e., the spatial heterogeneity of the tower surrounding area), was mostly negative around the tower during the greenup stage when the canopy of deciduous trees has not yet fully emerged yet (Fig. 6). The ΔEVI slightly increased at a window width of 250 m, including the conifer trees located on the northwest, northeast, and southeast sides of the tower (Fig. 1b), and then gradually converged to zero around a 1-km window width. Overall, the variations in the ΔEVI during the greenup stage were relatively small (less than 0.05) regardless of window widths. Meanwhile, the ΔEVI during the maturity and senescence stages revealed strong spatial heterogeneity around the tower. The ΔEVI values were higher than zero during the maturity stage (i.e. the averaged EVI around the tower was up to 16% higher than the magnitude of $\overline{EVI}_{1km}$), and then gradually converged to zero at the window widths of 700 and 500 m during the maturity and senescence stages, respectively (Fig. 6). The development of the southeast-side wetland has gradually decreased the ΔEVI at a window width between 250 and 500 m during the maturity stage.

399 *3.4. Significance of flux source attributes*

400 Over an entire growing season, the measured NEE was significantly correlated with both
401 vegetation density measures (R^2_{adj} = 0.48 and 0.55 with $\overline{EVI}_{1km}$ and $EVI_{\varphi 80}$, respectively, $p <$
402 0.01; Fig. 7). At a seasonal time scale, the correlations were still high for the greenup and
403 senescence stages (R^2_{adj} = 0.45-0.61, $p < 0.01$), but substantially weakened during the maturity
404 stage (R^2_{adj} = 0.01, $p > 0.1$; R^2_{adj} = 0.16, $p < 0.01$). Instead, for most of the meteorological classes,
405 the variation in the daytime NEE during the maturity stage was more accounted for by the
406 variation in the footprint-weighted land cover proportions ($P_{\varphi 80}$; Fig. 8b). The R^2_{adj} values from
407 the multiple linear regression with $P_{\varphi 80}$ were higher than the R^2_{adj} values from the OLS
408 regression with $EVI_{\varphi 80}$ for a higher number of meteorological classes than the number of classes
409 with the opposite R^2_{adj} values. On the other hand, the daytime NEE during the greenup and
410 senescence stages was poorly correlated with the $P_{\varphi 80}$ ($R^2_{adj} < 0.4$), and rather strongly driven by
411 $EVI_{\varphi 80}$ (R^2_{adj} up to 0.7) for some meteorological classes. The nighttime NEE was not well
412 correlated with either the $P_{\varphi 80}$ or the $EVI_{\varphi 80}$ ($R^2_{adj} < 0.4$) regardless of phenological stage for
413 most of the meteorological classes (Fig. 8d-f). The $P_{\varphi 80}$ of DBF was the significant factor for
414 most conditions (median *p*-value of all classes < 0.01; Fig. S10a), except for the greenup daytime
415 (median *p*-value of all classes = 0.06), even when the correlation was weak. The $P_{\varphi 80}$ of the
416 other land covers, on the other hand, was mostly non-significant. During the daytime, the
417 coefficient of $P_{\varphi 80}$ of DBF was more negative than that of ENF during the maturity and
418 senescence stages, less negative during the greenup stage (Fig. 9). During the nighttime, it was
419 more positive than that of ENF regardless of the phenological stage (Fig. 9).
420

4. Discussion

The study tower is located in a mixed forest where the landscape has gradually changed over the last decades, most noticeably with the expansion of two wetlands on the northwest and southeast sides from the tower (Fig. S7). Our principal goal in this study was to examine the spatial heterogeneity of the two surrounding spatial grid cells (1-km and 1.5-km) and the representativeness of the flux source area in capturing the vegetation characteristics (density magnitude and variation) of the two surrounding grid cells during the daytime and nighttime, respectively, during each phenological stage (greenup, maturity, and senescence). As expected, the study site was mostly homogeneous during the maturity stage in the early 1990s, as the deciduous trees had fully developed to a closed canopy (Lévesque and King, 1999). The expansion of two woody wetlands then began to impact the closed canopy, increasing spatial heterogeneity within the 1-km grid cell, resulting in with up to 3.5 times higher *sill* values than those associated with the canopy in the early 1990s (Fig. 5b). However, their proportion in the flux source areas were still less than 5%. This explains why the flux measurements (i.e., NEE) were not very sensitive to this variability (median *p*-value of all classes > 0.05; Fig. S10). The impact of the changing landscape was also very dependent on its spatial scale. The landscape within the 1.5-km grid cell was already highly heterogeneous in the 1990s, so there was a less of a noticeable change in the seasonal patterns of the *sill* values over the study period (Fig. 5b). Daytime flux source weights mostly peaked along the southwest side around the tower and did not exceed the 1-km grid cell, while the nighttime flux source areas covered larger areas (Fig. 3). Both daytime and nighttime flux source areas were dominated by DBF regardless of the phenological stage, but the proportion of DBF during the nighttime was smaller and more variable than the proportion during the daytime (Fig. 4). Our results suggest that the daytime flux

source areas cover a large enough area to adequately represent the vegetation density characteristics (distributions and magnitudes; Fig. 5c and Fig. 6, respectively) within the 1-km grid cell, but not those within the 1.5-km grid cell because of the additional non-vegetated land cover types at the northeastern corner of the grid cell (Fig. 1b). The vegetation density measures ($\overline{EVI}_{1km}$ and $EVI_{\varphi 80}$), therefore, were well correlated with the daytime NEE except during the maturity stage (Fig. 7 and Fig. 8a-c). During the maturity stage, on the other hand, the variations in the footprint-weighted land cover proportions ($P_{\varphi 80}$) accounted for higher proportions of the variations in the daytime NEE for most meteorological classes (Fig. 8b). Meanwhile, the nighttime NEE had little correlation with either vegetation density ($EVI_{\varphi 80}$) or the land cover ($P_{\varphi 80}$) regardless of the phenological stages (Fig. 8d-f), perhaps suggesting that these factors do not account for much of the variation in soil respiration, which is the dominant component of nighttime ecosystem respiration.

4.1. Study site spatial characteristics and flux source area representativeness

The *nugget effect* values of the 1-km grid cell reached almost zero during the entire growing season (Fig. 5a), which indicates that the sampling interval (i.e. 30 m of Landsat spatial resolution in this study) is appropriate to resolve the sources of spatial variation within the grid cell. Therefore, the Landsat data used in this study was suitable to assess the spatial representativeness of daytime flux source areas within the 1-km grid cell (Fig. 3). Nighttime flux source areas, however, often extended over a larger area under stable atmospheric conditions (Hadley and Schedlbauer, 2002; Kljun et al., 2002), therefore the 1.5-km surrounding area may be more applicable for the calibration and evaluation of lower resolution remote sensing-based

estimates. However, the increased *nugget effect* values of the 1.5-km grid cell during the maturity and senescence stages (almost 10% of the *sill* values) indicate that the spatial representativeness of the 1.5-km grid cell needs be assessed using a higher-spatial resolution data (e.g., higher resolution satellite imagery or aerial photographs) that are able to resolve the finer scale surface structures.

The *range* value can be considered to represent the effective size of the heterogeneity attributes (Kim et al., 2006). When a source area size (i.e., in this study, the geometric mean of along-wind and crosswind distances) is larger than the *range* value of the study grid cell, it can be assumed that the source area was large enough to represent the vegetation density variation in the study grid cell, and therefore, the source area is spatially-representative of the study grid cell (Kim et al., 2006). Over the study period, the *range* values of the 1-km grid cell were mostly less than or very close to the daytime source area extent throughout the entire growing season, and consistently smaller than the nighttime source area extent (Fig. 5c). This suggests that both the daytime and nighttime NEE measurements sufficiently reflect the variations in the vegetation density within the 1-km grid cell. The same interpretation can be applied for the 1.5-km grid cell during the daytime, but not during the nighttime when the *range* values mostly exceeded the source area extent.

The window size analysis generally corresponds with the semi-variogram results. The vegetation density around the tower is more heterogeneous than the density of the 1-km grid cell during the maturity stage, and smallest during the greenup stage (Fig. 6). The ΔEVI values are less than 5% of the 1-km average magnitudes within the source area during both the daytime and nighttime. This indicates that the source areas are generally large enough to represent the

magnitude of the vegetation density within the 1-km grid cell during both the daytime and nighttime.

4.2. Significance of footprint-weighted land cover proportion

As stated, the source areas were spatially representative of both vegetation density variations and magnitudes within the 1-km grid cell during both the daytime and nighttime across all phenological stages. Therefore, the 1-km grid cell mean EVI ($\overline{EVI}_{1km}$), as well as MODIS 1-km EVI (Rahman et al., 2005; Tang et al., 2011; Xiao et al., 2004), can adequately account for the variation in the daytime NEE as much as the footprint-weighted EVI ($EVI_{\varphi 80}$) can (Fig. 7). Specifically, the high correlations between the vegetation density measures ($\overline{EVI}_{1km}$ and $EVI_{\varphi 80}$) and the daytime NEE were primarily driven by the phenological development of the deciduous trees during the entire growing season and particularly during the greenup and senescence stages (EVI rises/drops by about 0.4). Therefore, the land cover variations within the source area had little effect on the daytime NEE during those periods. However, both $\overline{EVI}_{1km}$ and $EVI_{\varphi 80}$ can hardly account for the variation in the daytime NEE during the maturity stage, when both DBF and ENF have similar EVI values (Fig. 1c), and the vegetation carbon uptake primarily depends on its physiological response to meteorological variables, such as solar radiation, temperature, and soil moisture (Gao et al., 2014; Jahan and Gan, 2009; Tang et al., 2012). Yet, however, the mean response functions of a single vegetation functional type (DBF) accounted for only about 50% of the interannual variations in the NEE at the study site (Urbanski et al., 2007). Our results may provide a better explanation of the variation in the daytime NEE especially during foliage maturity (Fig. 8b). It was expected that

510 the $P_{\varphi 80}$ of DBF is the most significant factor in the flux measurements at the study tower, given
511 the dominance of DBF around the study tower (Urbanski et al., 2007), but it hadn't yet been
512 quantitatively assessed for each phenological stage. The stronger contribution of the $P_{\varphi 80}$ of
513 DBF (a more negative coefficient; Fig. 9) than that of ENF corresponds well to the higher carbon
514 uptake rates of deciduous trees than the ones of coniferous trees during the maturity stage
515 (Hadley et al., 2008). Although the $P_{\varphi 80}$ of ENF was not a significant factor on the daytime NEE
516 across the phenological stages, the greater negative coefficient of the $P_{\varphi 80}$ of ENF (representing
517 a stronger contribution) during the greenup stage than that of DBF reflects the higher carbon
518 uptake rates of the ENF than the DBF at the study site at the beginning of the growing season
519 (Hadley et al., 2008). The similar coefficient values of the $P_{\varphi 80}$ for both the DBF and ENF
520 during the senescence stage (Fig. 9) may result from the strong regulation of other factors, such
521 as day length (Bauerle et al., 2012) and soil moisture (Hwang et al., 2014; Urbanski et al., 2007),
522 rather than by leaf presence at the end of growing season.

523 Meanwhile, although the variations in the source area during the nighttime were higher
524 than those during the daytime, the nighttime NEE was only rather weakly correlated with either
525 $EVI_{\varphi 80}$ or $P_{\varphi 80}$ across all phenological stages. This could be largely attributed to the similar
526 rates of soil respiration at both DBF and ENF at the study site (Giasson et al., 2013).

527 Note that the significances and sensitivities of the measured NEE to the footprint-
528 weighted land cover proportions ($P_{\varphi 80}$; Eq. (4)) are subject to uncertainties in the NLCD
529 products and also to the limited NLCD availability (only 3 products over the 13 years study
530 period).

531

4.3. Implication for gap-filling process and upscaling strategies

To date the most common practice for filling gaps in hourly NEE measurements is to derive estimates from mean temperature- and light-response functions (Falge et al., 2001). Uncertainty is therefore introduced because those response functions are not intended to respond to the short-time variations in the meteorological drivers, but to characterize the ecosystem-scale mean response for a certain time period (in days or weeks) (Falge et al., 2001; Stoy et al., 2006). The isotopic eddy covariance flux data also showed that the ecosystem respiration values at the study tower were dependent on the wind direction, the therefore the source area variations (Wehr and Saleska, 2015). Our result indicates the dependence of the daytime NEE on the footprint-weighted land cover variations during the maturity stage, and addresses potential biases resulting from a discrepancy between the spatiotemporally-integrated mean ecosystem and the hourly-varying flux source areas. Therefore, this could cause misinterpretations of ecosystem short-term sensitivity to climate change and to the biome characteristics across multiple sites. In practice, it remains difficult to separate the flux measurements by upwind land cover types because it introduces additional uncertainties as the number of points in each bin available for calibration is substantially reduced. However, our analyses highlight the importance of considering the unique site-specific landscape conditions in the gap-filling process, especially during the peak growing season (i.e. the maturity stage) (Falge et al., 2001; Moffat et al., 2007).

Previous studies have investigated the implication of the source area variation on upwind vegetation density and meteorological factors when upscaling the measured flux to regional scales (Fu et al., 2014; Xu et al., 2017). However, vegetation dynamics (such as photosynthesis and respiration) do not necessarily respond linearly to these individual drivers (Urbanski et al., 2007), especially in water-limited ecosystems (Novick et al., 2015), and in dense canopies during

555 the peak growing season when the canopy is fully developed (Fig. 7; Urbanski et al., 2007). The
556 vegetation response to these drivers also varies greatly between the vegetation types (Daley et al.,
557 2007; Hadley et al., 2008). Therefore, in the process of calibrating the upscaling coefficients
558 using flux measurements, the source weight should be applied to the vegetation response (i.e. the
559 flux) depending on its type, rather than on its individual flux source attributes (i.e. vegetation
560 density or meteorological factors). The coefficient of the multiple linear regression, i.e., the NEE
561 rate per unit land cover proportion (g C m^{-2} s^{-1} $\%^{-1}$) for the given meteorological class, can be up-
562 scaled using the proportions of the significant land covers within the grid cell of interest (e.g. 1-
563 km).
564

565 ## 5. Conclusion

566 We assessed the long-term spatial heterogeneity around the study flux tower using remote
567 sensing datasets, and examined the representativeness of the flux measurements for the
568 surrounding area (1-km and 1.5-km grid cells, respectively) during the daytime and nighttime,
569 respectively, during each phenological stage (greenup, maturity, and senescence). In our study
570 site, the forested landscape had gradually shifted since 2001, resulting in an increase in spatial
571 heterogeneity within the 1-km grid cell centered at the flux tower, especially during the maturity
572 stage. Yet, the daytime flux source area remained spatially representative for vegetation
573 characteristics (both density and type) within this 1-km grid cell over the course of various
574 landscape transitions. We have demonstrated that the relevant flux source attribute, governing
575 more variation in the NEE, differed between phenological stages. The variation in the daytime
576 NEE is highly correlated with the vegetation density (EVI in this study) during the phenological
577 transition stages (greenup and senescence), but the variation during the maturity stage was better

captured by the footprint-weighted land cover proportion. The nighttime NEE was hardly affected by the variation in either the vegetation density or the land cover proportion.

Our study highlights the importance of accounting for variation in the footprint-weighted land cover in mixed-land cover regions (1) for interpretation of variations in flux measurements, (2) to fill data gaps, and (3) to upscale the flux measurements to larger scales. In this study, we only analyzed flux measurements from a single tower site (the tower that provides the longest flux record in the US) as a case study. Our approach can be further applied to other existing tower sites as there are increasing numbers of flux towers with multi-decadal flux measurements. Our results suggest a consideration of the land cover variations contributing to the measured flux will result in a better understanding of ecosystem response to environmental forcing in a changing climate.

Acknowledgements

The authors are grateful for the two anonymous reviewers whose comments have greatly improved the manuscript. We appreciate the efforts of Taejin Park in providing the processed LVIS data. We also would like to thank Dr. Miguel O. Roman for sharing the detailed methodology of semi-variogram analysis using Landsat data and Dr. Kimberly Novick for constructive comments on an earlier version of the manuscript. This study was financially supported in part by the NASA MODIS science team (Grant No. NNX11AD58G), the NASA Carbon Science program (Grant No. NNX17AE69G), and the USGS Science Team (Grant No. ING12PC00072). The Harvard Forest EMS flux tower has been supported by the Office of Science (BER) at the US Department of Energy (DOE) under various sub-programs over the years, and it is now a core site in AmeriFlux network (Grant No. DE-AC02-05CH11231). The

long-term meteorological and hydrological measurements at Harvard Forest are also supported through the National Science Foundation Long-Term Ecological Research Programs (Grant No. NSF-DEB-1237491). The Harvard Forest LTER data were obtained from the archive at (http://harvardforest.fas.harvard.edu/harvard-forest-data-archive).

Appendix A. Supplementary data

Supplementary material related to this article can be found, in the online version, at

Figures

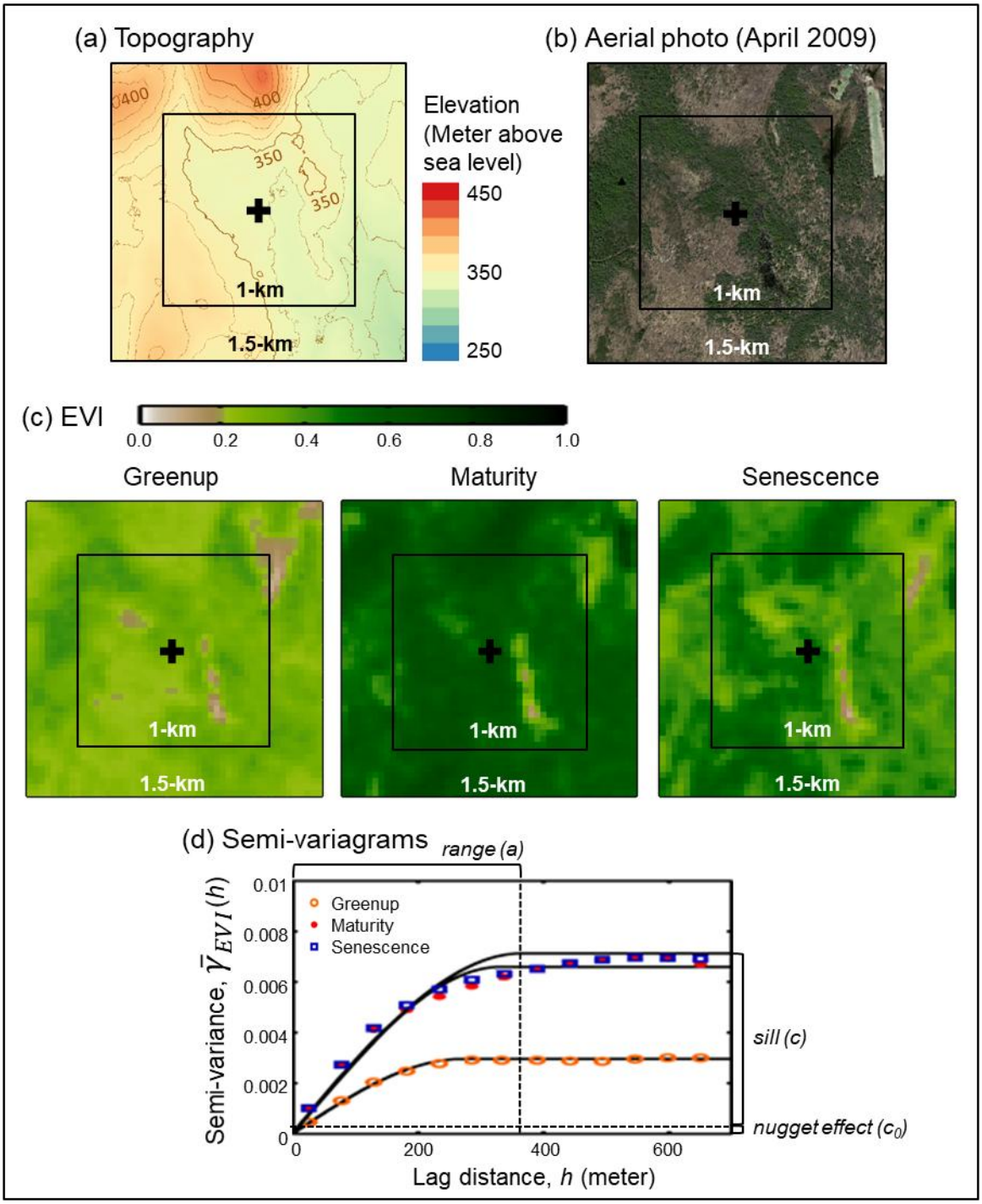

Fig. 1. (a) Topography of the surrounding area of the study tower (black cross). Elevation above sea level was retrieved from a LiDAR terrain file (accuracy of 5-35 cm; MassGIS: http://www.mass.gov/) (b) Aerial photo taken on April 2009 (30 cm resolution; MassGIS: http://www.mass.gov/) before the emergence of leaves on deciduous trees. (c) Enhanced vegetation index (EVI; Eq. (2)) maps retrieved from Landsat TM/ETM+ scenes at each phenological stage: greenup (5/27/2008), maturity (8/31/2008) and senescence (10/18/2008).

Details of the phenological stages are described in the data overview. (d) Schematic diagram of the semi-variogram estimators ($\bar{\gamma}_{EVI}(h)$) calculated from the EVI maps in (c) (orange circle, red dot, and blue square for greenup, maturity, and senescence stages, respectively), and the fitted isotropic spherical variogram models (black solid line), and *range*s (dashed vertical lines in colors).

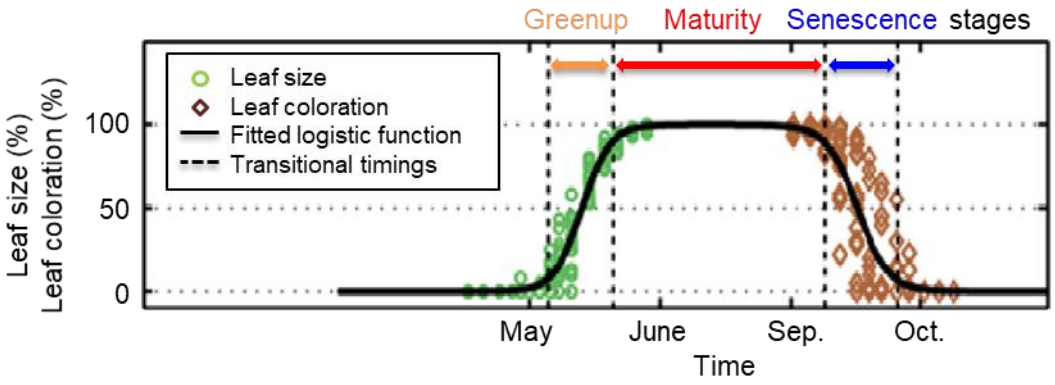

Fig. 2. Schematic diagram of estimating phenological stages. Leaf size and coloration data (green circles and brown diamonds) are based on ground-based visual observations (O'Keefe, 2000; data shown here is of 2008). A logistic function (Eq. (1)) is fitted to the indices for leaf size and coloration data, respectively (black solid line). Phenological stages (greenup, maturity, and senescence) are the periods between the phenological transitional timings (the dates when the curvature of the fitted function have the greatest changes; vertical dashed line).

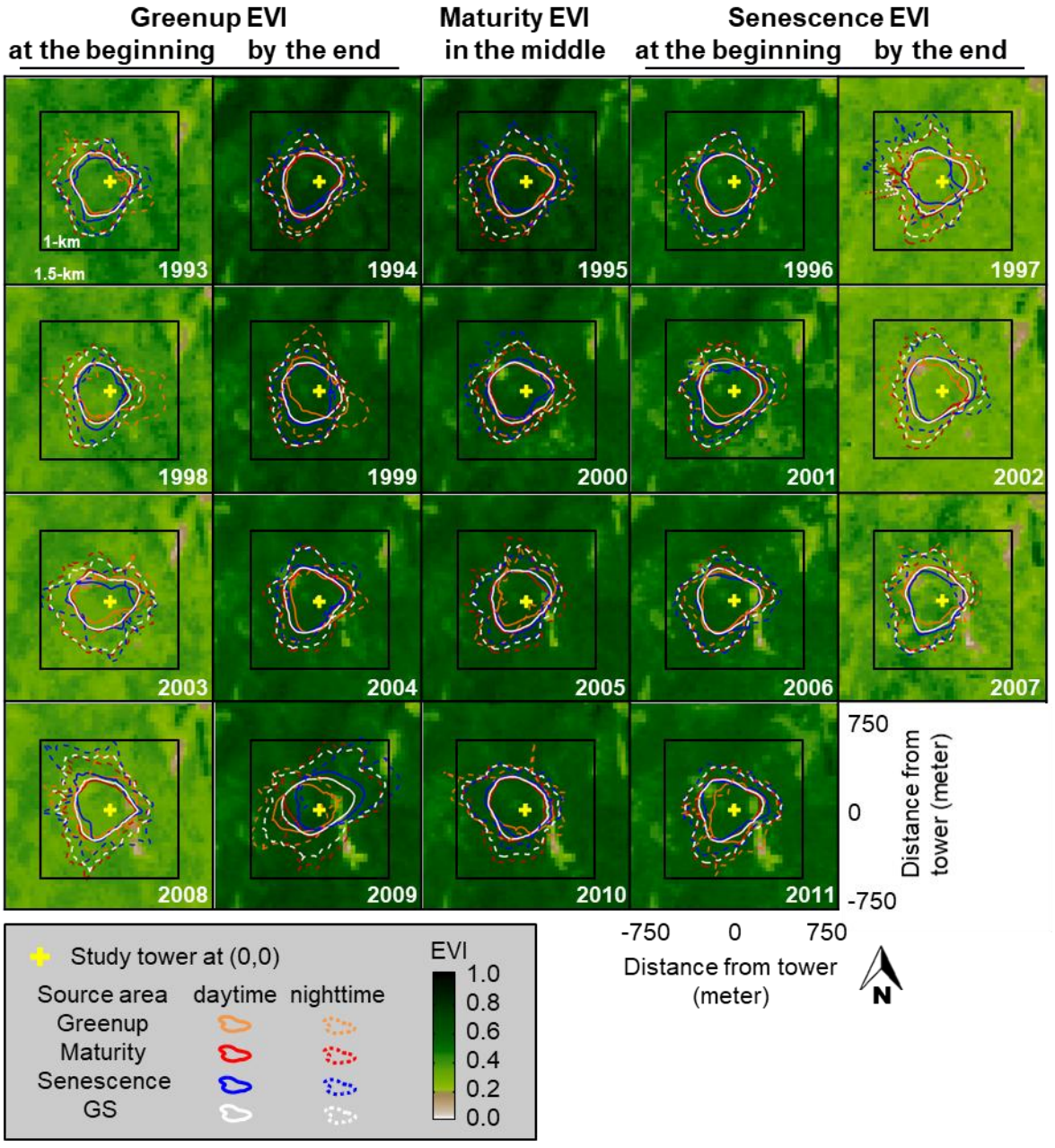

Fig. 3. Footprint climatology (i.e., an aggregation of source areas) during the daytime and nighttime (solid and dashed contours, respectively) during each phenological stage (greenup, maturity, senescence, and growing season, GS) from 1993 to 2011 overlaid on 1.5-km grid cell EVI maps centered at the study tower (yellow cross). EVI maps during the greenup stage are shown in the first and second columns, maturity stage in the third column, and senescence stage in the fourth and fifth columns.

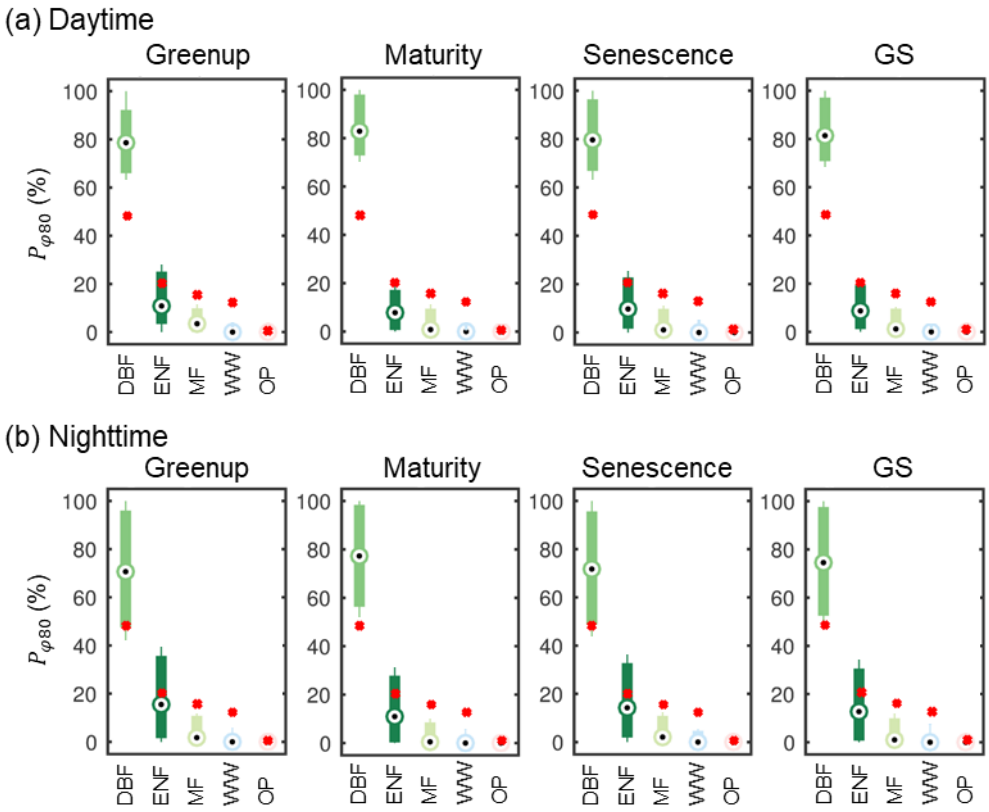

639

640 **Fig. 4.** The footprint-weighted proportions ($P_{\varphi 80}$; Eq. (4)) of each land cover (deciduous
641 broadleaf forest (DBF), evergreen needleleaf forest (ENF), mixed forest (MF), woody wetland
642 (WW), and open space area (OP) during the daytime (a) and the nighttime (b) during greenup,
643 maturity, and senescence stages, and during entire growing season (GS) from 1999 to 2011. The
644 box shows upper and lower quartile range of the $P_{\varphi 80}$ and the black dots represent the median
645 values. The average value of the nominal proportions of each land cover within the 1-km grid
646 cell in the NLCD products is marked as a red dot. The hourly $P_{\varphi 80}$ during each phenological
647 stage can be found in Fig. S9.

648

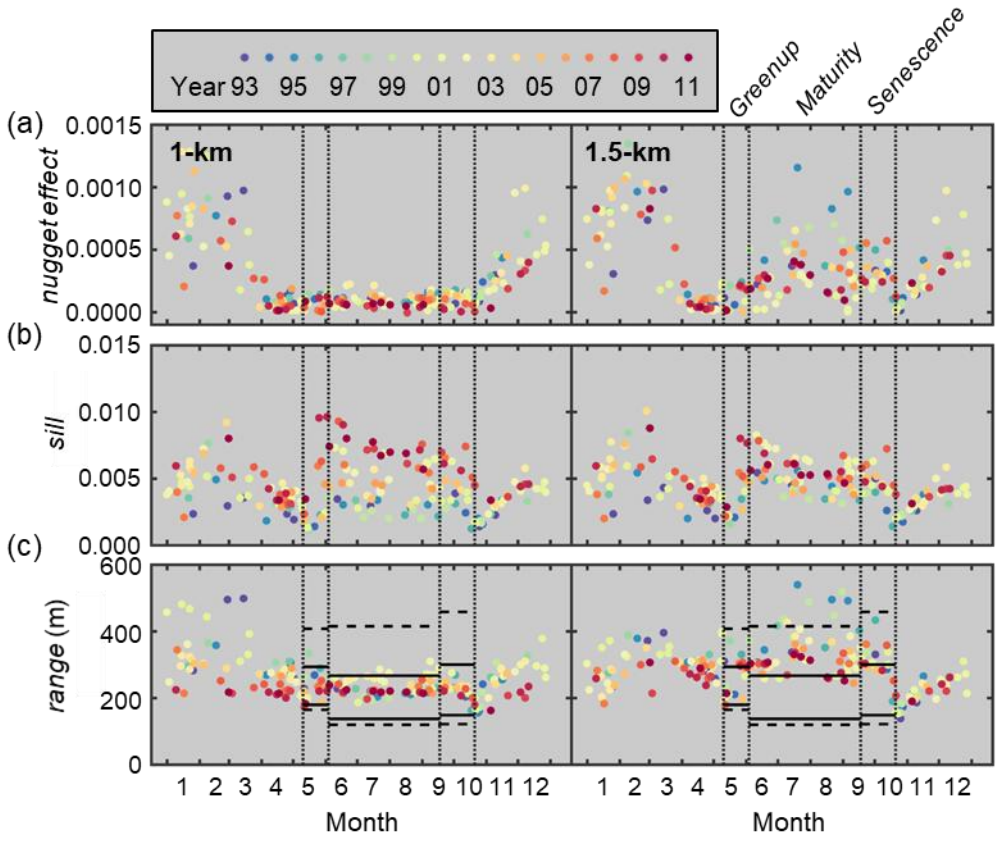

649

650 **Fig. 5.** Semi-variogram parameters, the *nugget effect* (a), *sill* (b), and *range* (c), derived from
651 EVI within 1-km (left panels) and 1.5-km (right panels) grid cells from 1993 to 2011 (in
652 different colors). One standard deviation of the geometric mean value of along-wind and
653 crosswind distances during the daytime and nighttime (horizontal solid and dashed lines,
654 respectively) is presented in the *range* plot (c) during each phenological stage (greenup,
655 maturity and senescence).

656

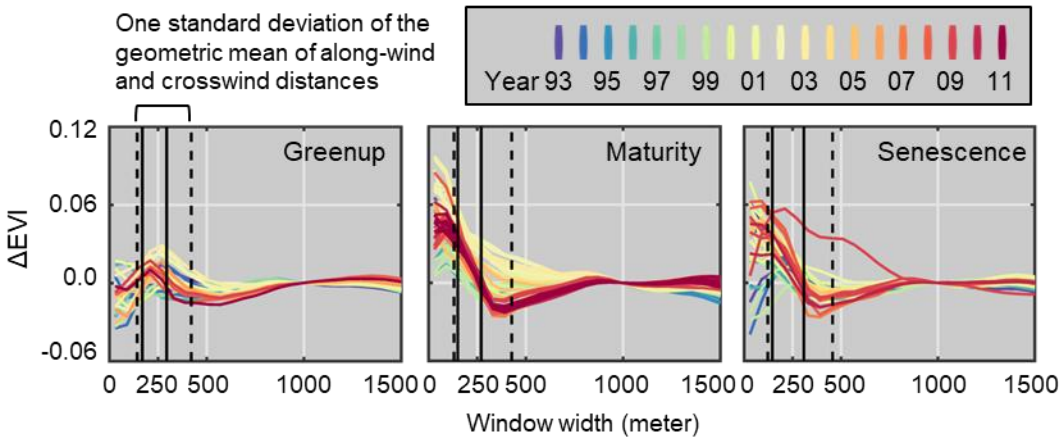

Fig. 6. The window-averaged EVI difference from the 1-km grid cell mean EVI (ΔEVI; Eq. (7)) between 1993 and 2011 (in different colors) during greenup, maturity, and senescence stages, respectively. One standard deviation of the geometric mean of along-wind and crosswind distances during the daytime and nighttime for each phenological stage is presented in vertical solid and dashed lines, respectively.

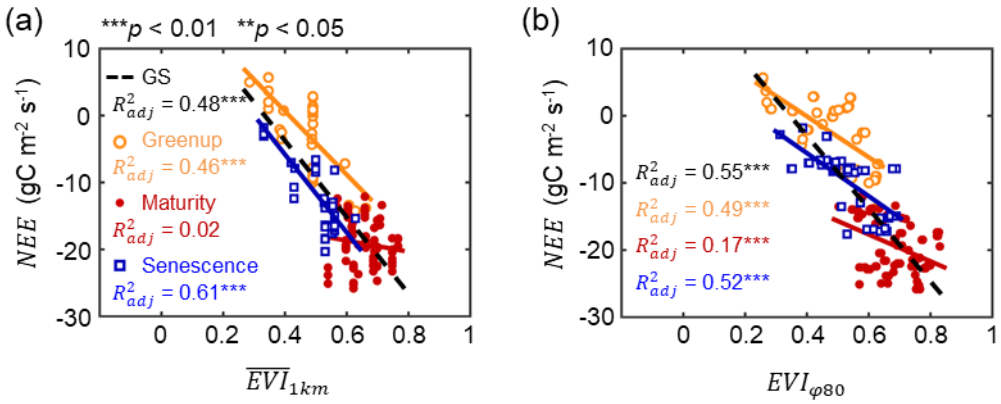

664

665 **Fig. 7.** The ordinary least squares (OLS) regressions between NEE and (a) the 1-km grid cell
666 mean EVI ($\overline{EVI}_{1km}$), and (b) the footprint-weighted EVI ($EVI_{\varphi 80}$) during entire growing season
667 (GS), and during greenup, maturity and senescence stages for a meteorological condition
668 (temperature, VPD, and PAR beyond the 75th percentile value of its cumulative distribution
669 function; Fig. S4).

670

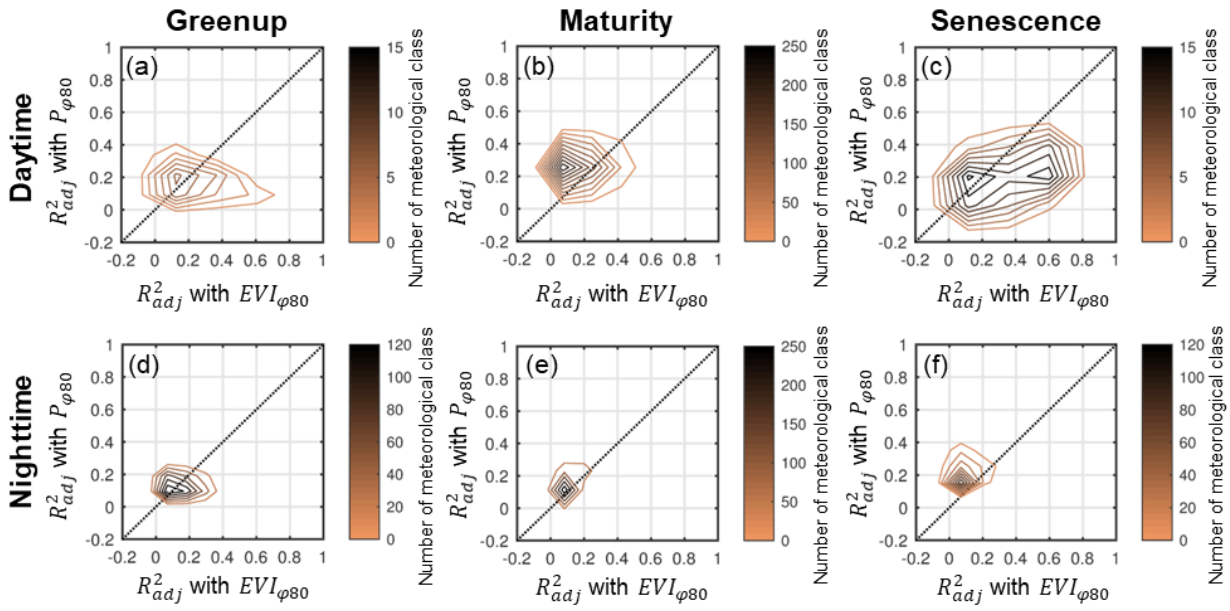

Fig. 8. Comparison of the adjusted coefficient of determination (R^2_{adj}) from the ordinary least square regression between NEE and footprint-weighted EVI ($EVI_{\varphi 80}$ in Eq. (3)) versus the R^2_{adj} from the multiple linear regression between NEE and footprint-weighted land cover proportions ($P_{\varphi 80}$; Eq. (4)) for the same meteorological class. The number of meteorological class having the R^2_{adj} values is shown in colored contours for each phenological stage (greenup on the first column, maturity on the second column, and senescence on the last column) during the daytime (a-c; PAR > 50 µmol m^{-2} s^{-1}) and nighttime (d-f), respectively.

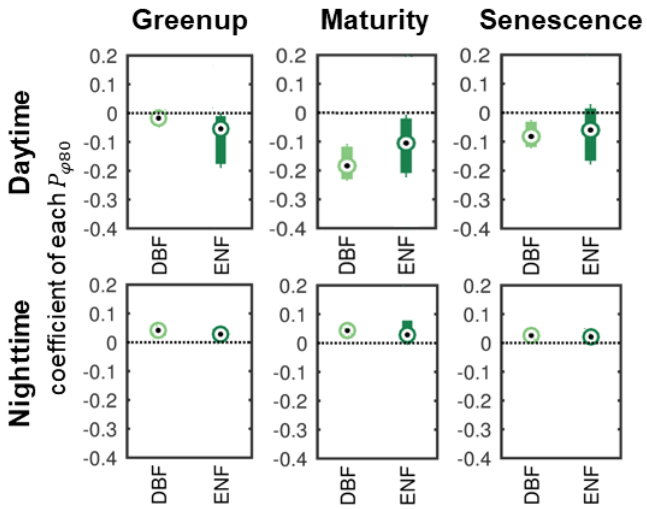

682

683 **Fig. 9.** The coefficients (i.e. NEE rate per unit land cover proportion (g C m^{-2} s^{-1} $\%^{-1}$)) of the two
684 most dominant land covers (deciduous broadleaf forest (DBF) and evergreen needleleaf forest
685 (ENF)) in the multiple linear regression between NEE and footprint-weighted land cover ($P_{\varphi 80}$)
686 (Eq. (8)). The coefficients of the non-dominant land covers (mixed forest and woody wetland;
687 each $P_{\varphi 80}$ < 5%) are presented in Fig. S10b. The regression was applied on each meteorological
688 class for each phenological stage (greenup, maturity, and senescence) during the daytime
689 (photosynthetically active radiation, PAR > 50 µmol m^{-2} s^{-1}) and nighttime, respectively. The
690 box shows upper and lower quartile range of the coefficients from all meteorological classes and
691 the black dots represent the median values.

692

Reference

Amiro, B.D., 1998. Footprint climatologies for evapotranspiration in a boreal catchment. Agric. For. Meteorol. 90, 195–201. doi:10.1016/S0168-1923(97)00096-8

Baldocchi, D.D., 2003. Assessing the eddy covariance technique for evaluating carbon dioxide exchange rates of ecosystems: past, present and future. Glob. Chang. Biol. 9, 479–492. doi:10.1046/j.1365-2486.2003.00629.x

Baldocchi, D.D., Hincks, B.B., Meyers, T.P., 1988. Measuring Biosphere-Atmosphere Exchanges of Biologically Related Gases with Micrometeorological Methods. Ecology 69, 1331. doi:10.2307/1941631

Battles, J.J., Robards, T., Das, A., Waring, K., Gilless, J.K., Biging, G., Schurr, F., 2007. Climate change impacts on forest growth and tree mortality: A data-driven modeling study in the mixedconifer forest of the Sierra Nevada, California. Clim. Change 87. doi:10.1007/s10584-007-9358-9

Bauerle, W.L., Oren, R., Way, D.A., Qian, S.S., Stoy, P.C., Thornton, P.E., Bowden, J.D., Hoffman, F.M., Reynolds, R.F., 2012. Photoperiodic regulation of the seasonal pattern of photosynthetic capacity and the implications for carbon cycling. Proc. Natl. Acad. Sci. U. S. A. 109, 8612–8617. doi:DOI 10.1073/pnas.1119131109

Belmecheri, S., Maxwell, R.S., Taylor, A.H., Davis, K.J., Freeman, K.H., Munger, J.W., 2014. Tree-ring δ 13 C tracks flux tower ecosystem productivity estimates in a NE temperate forest. Environ. Res. Lett. 9, 74011. doi:10.1088/1748-9326/9/7/074011

Cao, M., Woodward, F.I., 1998. Dynamic responses of terrestrial ecosystem carbon cycling to global climate change. Nature 393, 249–252. doi:10.1038/30460

Carroll, S.S., Cressie, N., 1996. A COMPARISON OF GEOSTATISTICAL METHODOLOGIES USED TO ESTIMATE SNOW WATER EQUIVALENT. J. Am. Water Resour. Assoc. 32, 267–278. doi:10.1111/j.1752-1688.1996.tb03450.x

Chasmer, L., Kljun, N., Hopkinson, C., Brown, S., Milne, B.T., Giroux, K., Barr, A.G., Devito, K.J., Creed, I.F., Petrone, R., 2011. Characterizing vegetation structural and topographic characteristics sampled by eddy covariance within two mature aspen stands using lidar and a flux footprint model: Scaling to MODIS. J. Geophys. Res. Biogeosciences 116, 1–19. doi:10.1029/2010JG001567

Chen, B., Coops, N.C., Fu, D., Margolis, H.A., Amiro, B.D., Barr, A.G., Black, T.A., Arain, M.A., Bourque, C.P.-A., Flanagan, L.B., Lafleur, P.M., McCaughey, H., Wofsy, S.C., 2011. Assessing eddy-covariance flux tower location bias across the Fluxnet-Canada Research Network based on remote sensing and footprint modelling. Agric. For. Meteorol. 151, 87–100. doi:10.1016/j.agrformet.2010.09.005

Chen, B., Coops, N.C., Fu, D., Margolis, H.A., Amiro, B.D., Black, T.A., Arain, M.A., Barr, A.G., Bourque, C.P.-A., Flanagan, L.B., Lafleur, P.M., McCaughey, H., Wofsy, S.C., 2012. Characterizing spatial representativeness of flux tower eddy-covariance measurements across the Canadian Carbon Program Network using remote sensing and footprint analysis. Remote Sens. Environ. 124, 742–755. doi:10.1016/j.rse.2012.06.007

Chen, B., Zhang, H., Coops, N.C., Fu, D., Worthy, D.E.J., Xu, G., Black, T.A., 2013. Assessing scalar concentration footprint climatology and land surface impacts on tall-tower CO2 concentration measurements in the boreal forest of central Saskatchewan, Canada. Theor. Appl. Climatol. 118, 115–132. doi:10.1007/s00704-013-1038-2

Curran, P., 1988. The semi-variogram in remote sensing: an introduction. Remote Sens. Environ.

507, 493–507. doi:10.1016/0034-4257(88)90021-1
Daley, M.J., Phillips, N.G., Pettijohn, C., Hadley, J.L., 2007. Water use by eastern hemlock (Tsuga canadensis) and black birch (Betula lenta): implications of effects of the hemlock woolly adelgid. Can. J. For. Res. 37, 2031–2040. doi:10.1139/X07-045
Davidson, E.A., Richardson, A.D., Savage, K.E., Hollinger, D.Y., 2006. A distinct seasonal pattern of the ratio of soil respiration to total ecosystem respiration in a spruce-dominated forest. Glob. Chang. Biol. 12, 230–239. doi:10.1111/j.1365-2486.2005.01062.x
Davis, J.C., 1986. Statistics and Data Analysis in Geology, Volume 1. Wiley.
Falge, E.M., Baldocchi, D.D., Olson, R., Anthoni, P., Aubinet, M., Bernhofer, C., Burba, G., Ceulemans, R., Clement, R., Dolman, H., Granier, A., Gross, P., Grünwald, T., Hollinger, D.Y., Jensen, N.-O., Katul, G.G., Keronen, P., Kowalski, A.S., Lai, C.T., Law, B.E., Meyers, T.P., Moncrieff, J., Moors, E., Munger, J.W., Pilegaard, K., Rannik, Ü., Rebmann, C., Suyker, A., Tenhunen, J., Tu, K., Verma, S.B., Vesala, T., Wilson, K.B., Wofsy, S.C., 2001. Gap filling strategies for defensible annual sums of net ecosystem exchange. Agric. For. Meteorol. 107, 43–69. doi:10.1016/S0168-1923(00)00225-2
Falge, E.M., Baldocchi, D.D., Tenhunen, J., Aubinet, M., Bakwin, P., Berbigier, P., Bernhofer, C., Burba, G., Clement, R., Davis, K.J., Elbers, J.A., Goldstein, A.H., Grelle, A., Granier, A., Guðmundsson, J., Hollinger, D.Y., Kowalski, A.S., Katul, G.G., Law, B.E., Malhi, Y., Meyers, T.P., Monson, R.K., Munger, J.W., Oechel, W.C., Paw U, K.T., Pilegaard, K., Rannik, Ü., Rebmann, C., Suyker, A., Valentini, R., Wilson, K.B., Wofsy, S.C., 2002. Seasonality of ecosystem respiration and gross primary production as derived from FLUXNET measurements. Agric. For. Meteorol. 113, 53–74. doi:10.1016/S0168-1923(02)00102-8
Finzi, A.C., Austin, A.T., Cleland, E.E., Frey, S.D., Houlton, B.Z., Wallenstein, M.D., 2011. Responses and feedbacks of coupled biogeochemical cycles to climate change: examples from terrestrial ecosystems. Front. Ecol. Environ. 9, 61–67. doi:10.1890/100001
Fu, D., Chen, B., Zhang, H., Wang, J., Black, T.A., Amiro, B.D., Bohrer, G., Bolstad, P. V., Coulter, R., Rahman, A.F., Dunn, A.L., McCaughey, H., Meyers, T.P., Verma, S.B., 2014. Estimating landscape net ecosystem exchange at high spatial–temporal resolution based on Landsat data, an improved upscaling model framework, and eddy covariance flux measurements. Remote Sens. Environ. 141, 90–104. doi:10.1016/j.rse.2013.10.029
Gao, X., 2000. Optical–Biophysical Relationships of Vegetation Spectrca without Background Contamination. Remote Sens. Environ. 74, 609–620. doi:10.1016/S0034-4257(00)00150-4
Gao, Y., Yu, G., Yan, H., Zhu, X., Li, S., Wang, Q., Zhang, J., Wang, Y., Li, Y., Zhao, L., Shi, P., 2014. A MODIS-based Photosynthetic Capacity Model to estimate gross primary production in Northern China and the Tibetan Plateau. Remote Sens. Environ. 148, 108–118. doi:10.1016/j.rse.2014.03.006
Giasson, M.-A., Ellison, A.M., Bowden, R.D., Crill, P.M., Davidson, E.A., Drake, J.E., Frey, S.D., Hadley, J.L., Lavine, M., Melillo, J.M., Munger, J.W., Nadelhoffer, K.J., Nicoll, L., Ollinger, S. V., Savage, K.E., Steudler, P.A., Tang, J., Varner, R.K., Wofsy, S.C., Foster, D.R., Finzi, A.C., 2013. Soil respiration in a northeastern US temperate forest: a 22-year synthesis. Ecosphere 4, art140. doi:10.1890/ES13.00183.1
Göckede, M., Foken, T., Aubinet, M., Aurela, M., Banza, J., Bernhofer, C., Bonnefond, J.M., Brunet, Y., Carrara, A., Clement, R., Dellwik, E., Elbers, J., Eugster, W., Fuhrer, J., Granier, A., Grünwald, T., Heinesch, B., Janssens, I.A., Knohl, A., Koeble, R., Laurila, T., Longdoz, B., Manca, G., Marek, M., Markkanen, T., Mateus, J., Matteucci, G., Mauder, M.,

784 Migliavacca, M., Minerbi, S., Moncrieff, J., Montagnani, L., Moors, E., Ourcival, J.-M.,
785 Papale, D., Pereira, J., Pilegaard, K., Pita, G., Rambal, S., Rebmann, C., Rodrigues, A.,
786 Rotenberg, E., Sanz, M., Sedlak, P., Seufert, G., Siebicke, L., Soussana, J.F., Valentini, R.,
787 Vesala, T., Verbeeck, H., Yakir, D., 2008. Quality control of CarboEurope flux data – Part
788 1: Coupling footprint analyses with flux data quality assessment to evaluate sites in forest
789 ecosystems. Biogeosciences 5, 433–450. doi:10.5194/bg-5-433-2008
790 Goulden, M.L., Munger, J.W., Fan, S.-M., Daube, B.C., Wofsy, S.C., 1996. Measurements of
791 carbon sequestration by long-term eddy covariance: methods and a critical evaluation of
792 accuracy. Glob. Chang. Biol. 2, 169–182. doi:10.1111/j.1365-2486.1996.tb00070.x
793 Griebel, A., Bennett, L.T., Metzen, D., Cleverly, J., Burba, G., Arndt, S.K., 2016. Effects of
794 inhomogeneities within the flux footprint on the interpretation of seasonal, annual, and
795 interannual ecosystem carbon exchange. Agric. For. Meteorol. 221, 50–60.
796 doi:10.1016/j.agrformet.2016.02.002
797 Hadley, J.L., Kuzeja, P.S., Daley, M.J., Phillips, N.G., Mulcahy, T., Singh, S., 2008. Water use
798 and carbon exchange of red oak- and eastern hemlock-dominated forests in the northeastern
799 USA: implications for ecosystem-level effects of hemlock woolly adelgid. Tree Physiol. 28,
800 615–627. doi:10.1093/treephys/28.4.615
801 Hadley, J.L., Schedlbauer, J.L., 2002. Carbon exchange of an old-growth eastern hemlock
802 (Tsuga canadensis) forest in central New England. Tree Physiol. 22, 1079–1092.
803 doi:10.1093/treephys/22.15-16.1079
804 Haylock, M.R., Hofstra, N., Klein Tank, a. M.G., Klok, E.J., Jones, P.D., New, M., 2008. A
805 European daily high-resolution gridded data set of surface temperature and precipitation for
806 1950-2006. J. Geophys. Res. Atmos. 113. doi:10.1029/2008JD010201
807 Heinsch, F.A., Maosheng Zhao, Running, S.W., Kimball, J.S., Nemani, R.R., Davis, K.J.,
808 Bolstad, P.V., Cook, B.D., Desai, A.R., Ricciuto, D.M., Law, B.E., Oechel, W.C., Hyojung
809 Kwon, Hongyan Luo, Wofsy, S.C., Dunn, A.L., Munger, J.W., Baldocchi, D.D., Liukang
810 Xu, Hollinger, D.Y., Richardson, A.D., Stoy, P.C., Siqueira, M.B.S., Monson, R.K., Burns,
811 S.P., Flanagan, L.B., 2006. Evaluation of remote sensing based terrestrial productivity from
812 MODIS using regional tower eddy flux network observations. IEEE Trans. Geosci. Remote
813 Sens. 44, 1908–1925. doi:10.1109/TGRS.2005.853936
814 Hsieh, C., Katul, G., Chi, T., 2000. An approximate analytical model for footprint estimation of
815 scalar fluxes in thermally stratified atmospheric flows. Adv. Water Resour. 23, 765–772.
816 doi:10.1016/S0309-1708(99)00042-1
817 Huete, A.R., Didan, K., Miura, T., Rodriguez, E.., Gao, X., Ferreira, L.., 2002. Overview of the
818 radiometric and biophysical performance of the MODIS vegetation indices. Remote Sens.
819 Environ. 83, 195–213. doi:10.1016/S0034-4257(02)00096-2
820 Hutjes, R.W.A., Vellinga, O.S., Gioli, B., Miglietta, F., 2010. Dis-aggregation of airborne flux
821 measurements using footprint analysis. Agric. For. Meteorol. 150, 966–983.
822 doi:10.1016/j.agrformet.2010.03.004
823 Hwang, T., Band, L.E., Miniat, C.F., Song, C., Bolstad, P. V., Vose, J.M., Love, J.P., 2014.
824 Divergent phenological response to hydroclimate variability in forested mountain
825 watersheds. Glob. Chang. Biol. 20, 2580–95. doi:10.1111/gcb.12556
826 Hwang, T., Song, C., Vose, J.M., Band, L.E., 2011. Topography-mediated controls on local
827 vegetation phenology estimated from MODIS vegetation index. Landsc. Ecol. 26, 541–556.
828 doi:10.1007/s10980-011-9580-8
829 Jahan, N., Gan, T.Y., 2009. Modeling gross primary production of deciduous forest using

remotely sensed radiation and ecosystem variables. J. Geophys. Res. 114, G04026. doi:10.1029/2008JG000919
Keenan, T.F., Gray, J., Friedl, M.A., Toomey, M., Bohrer, G., Hollinger, D.Y., Munger, J.W., O'Keefe, J., Schmid, H.P., Wing, I.S., Yang, B., Richardson, A.D., 2014. Net carbon uptake has increased through warming-induced changes in temperate forest phenology. Nat. Clim. Chang. 4, 598–604. doi:10.1038/nclimate2253
Keenan, T.F., Hollinger, D.Y., Bohrer, G., Dragoni, D., Munger, J.W., Schmid, H.P., Richardson, A.D., 2013. Increase in forest water-use efficiency as atmospheric carbon dioxide concentrations rise. Nature 499, 324–7. doi:10.1038/nature12291
Kim, J., Guo, Q., Baldocchi, D.D., Leclerc, M., Xu, L., Schmid, H.P., 2006. Upscaling fluxes from tower to landscape: Overlaying flux footprints on high-resolution (IKONOS) images of vegetation cover. Agric. For. Meteorol. 136, 132–146. doi:10.1016/j.agrformet.2004.11.015
Kim, J., Hwang, T., Schaaf, C.L., Orwig, D.A., Boose, E., Munger, J.W., 2017. Increased water yield due to the hemlock woolly adelgid infestation in New England. Geophys. Res. Lett. 2327–2335. doi:10.1002/2016GL072327
Kljun, N., Calanca, P., Rotach, M.W., Schmid, H.P., 2015. A simple two-dimensional parameterisation for Flux Footprint Prediction (FFP). Geosci. Model Dev. 8, 3695–3713. doi:10.5194/gmd-8-3695-2015
Kljun, N., Calanca, P., Rotach, M.W., Schmid, H.P., 2004. A simple parameterisation for flux footprint predictions. Boundary-Layer Meteorol. 112, 503–523. doi:10.1023/B:BOUN.0000030653.71031.96
Kljun, N., Rotach, M.W., Schmid, H.P., 2002. A Three-Dimensional Backward Lagrangian Footprint Model For A Wide Range Of Boundary-Layer Stratifications. Boundary-Layer Meteorol. 103, 205–226. doi:10.1023/A:1014556300021
Kormann, R., Meixner, F.X., 2001. An Analytical Footprint Model For Non-Neutral Stratification. Boundary-Layer Meteorol. 99, 207–224. doi:10.1023/A:1018991015119
Law, B.., Falge, E.M., Gu, L., Baldocchi, D.D., Bakwin, P., Berbigier, P., Davis, K., Dolman, A.., Falk, M., Fuentes, J.., Goldstein, A., Granier, A., Grelle, A., Hollinger, D., Janssens, I.., Jarvis, P., Jensen, N.., Katul, G., Mahli, Y., Matteucci, G., Meyers, T., Monson, R., Munger, J.W., Oechel, W.C., Olson, R., Pilegaard, K., Paw U, K.T., Thorgeirsson, H., Valentini, R., Verma, S., Vesala, T., Wilson, K.B., Wofsy, S., 2002. Environmental controls over carbon dioxide and water vapor exchange of terrestrial vegetation. Agric. For. Meteorol. 113, 97–120. doi:10.1016/S0168-1923(02)00104-1
Lévesque, J., King, D.J., 1999. Airborne digital camera image semivariance for evaluation of forest structural damage at an acid mine site. Remote Sens. Environ. 68, 112–124. doi:10.1016/S0034-4257(98)00104-7
Masek, J.G., Vermote, E.F., Saleous, N.E., Wolfe, R.E., Hall, F.G., Huemmrich, K.F., Gao, F., Kutler, J., Lim, T., 2006. A Landsat Surface Reflectance Dataset. IEEE Geosci. Remote Sens. Lett. 3, 68–72. doi:10.1109/LGRS.2005.857030
Matheron, G., 1963. Principles of geostatistics. Econ. Geol. 58, 1246–1266. doi:10.2113/gsecongeo.58.8.1246
Menzer, O., Pastorello, G., Metzger, S., Poindexter, C., Agarwal, D., Papale, D., 2014. Mapping AmeriFlux footprints: Towards knowing the flux source area across a network of towers, in: American Geophysical Union, Fall Meeting 2014, Abstract #B53A-0155.
Menzer, O., Pastorello, G., Metzger, S.R.I., Poindexter, C., Agarwal, D., Papale, D., 2015.

876 Mapping AmeriFlux footprints: Towards deconvolving spatial and temporal co-variation
877 across a network of flux towers, in: 5th NACP All-Investigators Meeting.
878 Moffat, A.M., Papale, D., Reichstein, M., Hollinger, D.Y., Richardson, A.D., Barr, A.G.,
879 Beckstein, C., Braswell, B.H., Churkina, G., Desai, A.R., Falge, E.M., Gove, J.H., Heimann,
880 M., Hui, D., Jarvis, A.J., Kattge, J., Noormets, A., Stauch, V.J., 2007. Comprehensive
881 comparison of gap-filling techniques for eddy covariance net carbon fluxes. Agric. For.
882 Meteorol. 147, 209–232. doi:10.1016/j.agrformet.2007.08.011
883 Munger, J.W., Wofsy, S.C., 1999a. Biomass Inventories at Harvard Forest EMS Tower since
884 1993. Environmental Data Initiative. [WWW Document].
885 doi:10.6073/pasta/8c1c49009eda396ae7ad48e2f0dd4eca
886 Munger, J.W., Wofsy, S.C., 1999b. Canopy-Atmosphere Exchange of Carbon, Water and Energy
887 at Harvard Forest EMS Tower since 1991. Environmental Data Initiative. [WWW
888 Document]. doi:10.6073/pasta/1580a910a8a1a154cb59c941b252613a
889 Nemani, R.R., Keeling, C.D., Hashimoto, H., Jolly, W.M., Piper, S.C., Tucker, C.J., Myneni,
890 R.B., Running, S.W., 2003. Climate-Driven Increases in Global Terrestrial Net Primary
891 Production from 1982 to 1999. Science (80-.). 300, 1560–1563.
892 doi:10.1126/science.1082750
893 Noréus, J.P., Nyborg, M.R., Hayling, K.L., 1997. The gravity anomaly field in the Gulf of
894 Bothnia spatially characterized from satellite altimetry and in situ measurements. J. Appl.
895 Geophys. 37, 67–84. doi:10.1016/S0926-9851(97)00007-4
896 Novick, K.A., Brantley, S.T., Miniat, C.F., Walker, J., Vose, J.M., 2014. Inferring the
897 contribution of advection to total ecosystem scalar fluxes over a tall forest in complex
898 terrain. Agric. For. Meteorol. 185, 1–13. doi:10.1016/j.agrformet.2013.10.010
899 Novick, K.A., Oishi, C.A., Ward, E.J., Siqueira, M.B.S., Juang, J.-Y., Stoy, P.C., Oishi, A.C.,
900 Ward, E.J., Siqueira, M.B.S., Juang, J.-Y., Stoy, P.C., 2015. On the difference in the net
901 ecosystem exchange of CO 2 between deciduous and evergreen forests in the southeastern
902 United States. Glob. Chang. Biol. 21, 827–842. doi:10.1111/gcb.12723
903 O'Keefe, J., 2000. Phenology of Woody Species at Harvard Forest since 1990. Environmental
904 Data Initiative. [WWW Document].
905 doi:10.6073/pasta/bf1e4d2f198ab9b02da82154236b0816
906 Oishi, C.A., Oren, R., Stoy, P.C., 2008. Estimating components of forest evapotranspiration: A
907 footprint approach for scaling sap flux measurements. Agric. For. Meteorol. 148, 1719–
908 1732. doi:10.1016/j.agrformet.2008.06.013
909 Orwig, D.A., Cobb, R.C., D'Amato, A.W., Kizlinski, M.L., Foster, D.R., 2008. Multi-year
910 ecosystem response to hemlock woolly adelgid infestation in southern New England forests.
911 Can. J. For. Res. 38, 834–843. doi:10.1139/X07-196
912 Park, T., Kennedy, R., Choi, S., Wu, J., Lefsky, M., Bi, J., Mantooth, J., Myneni, R., Knyazikhin,
913 Y., 2014. Application of Physically-Based Slope Correction for Maximum Forest Canopy
914 Height Estimation Using Waveform Lidar across Different Footprint Sizes and Locations:
915 Tests on LVIS and GLAS. Remote Sens. 6, 6566–6586. doi:10.3390/rs6076566
916 Pastorello, G., Agarwal, D., Papale, D., Samak, T., Trotta, C., Ribeca, A., Poindexter, C.,
917 Faybishenko, B., Gunter, D., Hollowgrass, R., Canfora, E., 2014. Observational Data
918 Patterns for Time Series Data Quality Assessment, in: Proceedings of the 2014 IEEE 10th
919 International Conference on E-Science - Volume 01, E-SCIENCE '14. IEEE Computer
920 Society, Washington, DC, USA, pp. 271–278. doi:10.1109/eScience.2014.45
921 Phillips, S.C., Varner, R.K., Frolking, S., Munger, J.W., Bubier, J.L., Wofsy, S.C., Crill, P.M.,

2010. Interannual, seasonal, and diel variation in soil respiration relative to ecosystem respiration at a wetland to upland slope at Harvard Forest. J. Geophys. Res. 115, 1–18. doi:10.1029/2008JG000858

Rahman, A.F., Sims, D.A., Cordova, V.D., El-Masri, B.Z., 2005. Potential of MODIS EVI and surface temperature for directly estimating per-pixel ecosystem C fluxes. Geophys. Res. Lett. 32, n/a-n/a. doi:10.1029/2005GL024127

Román, M.O., Schaaf, C.L., Woodcock, C.E., Strahler, A.H., Yang, X., Braswell, B.H., Curtis, P.S., Davis, K.J., Dragoni, D., Goulden, M.L., 2009. The MODIS (Collection V005) BRDF/albedo product: Assessment of spatial representativeness over forested landscapes. Remote Sens. Environ. 113, 2476–2498. doi:10.1016/j.rse.2009.07.009

Schmid, H.P., 1997. Experimental design for flux measurements: matching scales of observations and fluxes. Agric. For. Meteorol. 87, 179–200. doi:10.1016/S0168-1923(97)00011-7

Schmid, H.P., 1994. Source areas for scalars and scalar fluxes. Boundary-Layer Meteorol. 67, 293–318. doi:10.1007/BF00713146

Schmid, H.P., Grimmond, C.S.B., Cropley, F.D., Offerle, B., Su, H.-B., 2000. Measurements of CO2 and energy fluxes over a mixed hardwood forest in the mid-western United States. Agric. For. Meteorol. 103, 357–374. doi:10.1016/S0168-1923(00)00140-4

Schmid, H.P., Lloyd, C.R., 1999. Spatial representativeness and the location bias of flux footprints over inhomogeneous areas. Agric. For. Meteorol. 93, 195–209. doi:10.1016/S0168-1923(98)00119-1

Schwalm, C.R., Williams, C. a., Schaefer, K., Anderson, R., Arain, M.A., Baker, I., Barr, A., Black, T.A., Chen, G., Chen, J.M., Ciais, P., Davis, K.J., Desai, A., Dietze, M., Dragoni, D., Fischer, M.L., Flanagan, L.B., Grant, R., Gu, L., Hollinger, D., Izaurralde, R.C., Kucharik, C.J., Lafleur, P., Law, B.E., Li, L., Li, Z., Liu, S., Lokupitiya, E., Luo, Y., Ma, S., Margolis, H., Matamala, R., McCaughey, H., Monson, R.K., Oechel, W.C., Peng, C., Poulter, B., Price, D.T., Riciutto, D.M., Riley, W., Sahoo, A.K., Sprintsin, M., Sun, J., Tian, H., Tonitto, C., Verbeeck, H., Verma, S.B., 2010. A model-data intercomparison of CO 2 exchange across North America: Results from the North American Carbon Program site synthesis. J. Geophys. Res. 115, G00H05. doi:10.1029/2009JG001229

Stoy, P.C., Katul, G.G., Siqueira, M.B.S., Juang, J.-Y., Novick, K.A., Uebelherr, J.M., Oren, R., 2006. An evaluation of models for partitioning eddy covariance-measured net ecosystem exchange into photosynthesis and respiration. Agric. For. Meteorol. 141, 2–18. doi:10.1016/j.agrformet.2006.09.001

Stull, R.B., 1988. An Introduction to Boundary Layer Meteorology. Springer Netherlands, Dordrecht. doi:10.1007/978-94-009-3027-8

Susaki, J., Yasuoka, Y., Kajiwara, K., Honda, Y., Hara, K., 2007. Validation of MODIS albedo products of paddy fields in Japan. IEEE Trans. Geosci. Remote Sens. 45, 206–217. doi:10.1109/TGRS.2006.882266

Tang, X., Liu, D., Song, K., Munger, J.W., Zhang, B., Wang, Z., 2011. A new model of net ecosystem carbon exchange for the deciduous-dominated forest by integrating modis and flux data. Ecol. Eng. 37, 1567–1571. doi:10.1016/j.ecoleng.2011.03.030

Tang, X., Wang, Z., Liu, D., Song, K., Jia, M., Dong, Z., Munger, J.W., Hollinger, D.Y., Bolstad, P. V., Goldstein, A.H., Desai, A.R., Dragoni, D., Liu, X., 2012. Estimating the net ecosystem exchange for the major forests in the northern United States by integrating MODIS and AmeriFlux data. Agric. For. Meteorol. 156, 75–84.

968 doi:10.1016/j.agrformet.2012.01.003
969 Tian, Y., Woodcock, C.E., Wang, Y., Privette, J.L., Shabanov, N. V., Zhou, L., Zhang, Y.,
970 Buermann, W., Dong, J., Veikkanen, B., 2002. Multiscale analysis and validation of the
971 MODIS LAI productII. Sampling strategy. Remote Sens. Environ. 83, 431–441.
972 doi:10.1016/S0034-4257(02)00058-5
973 Trotter, R.T., Morin, R.S., Oswalt, S.N., Liebhold, A., 2013. Changes in the regional abundance
974 of hemlock associated with the invasion of hemlock woolly adelgid (Adelges tsugae
975 Annand). Biol. Invasions 15, 2667–2679. doi:10.1007/s10530-013-0482-3
976 Turner, D.P., Ritts, W.D., Cohen, W.B., Gower, S.T., Zhao, M., Running, S.W., Wofsy, S.C.,
977 Urbanski, S.P., Dunn, A.L., Munger, J.W., 2003. Scaling Gross Primary Production (GPP)
978 over boreal and deciduous forest landscapes in support of MODIS GPP product validation.
979 Remote Sens. Environ. 88, 256–270. doi:10.1016/j.rse.2003.06.005
980 Urbanski, S.P., Barford, C., Wofsy, S., Kucharik, C.J., Pyle, E., Budney, J., McKain, K.,
981 Fitzjarrald, D., Czikowsky, M.J., Munger, J.W., 2007. Factors controlling CO 2 exchange
982 on timescales from hourly to decadal at Harvard Forest. J. Geophys. Res. 112, G02020.
983 doi:10.1029/2006JG000293
984 van Ulden, A.P., 1978. Simple estimates for vertical diffusion from sources near the ground.
985 Atmos. Environ. 12, 2125–2129. doi:10.1016/0004-6981(78)90167-1
986 Verma, M., Friedl, M.A., Law, B.E., Bonal, D., Kiely, G., Black, T.A., Wohlfahrt, G., Moors,
987 E.J., Montagnani, L., Marcolla, B., Toscano, P., Varlagin, A., Roupsard, O., Cescatti, A.,
988 Arain, M.A., D'Odorico, P., 2015. Improving the performance of remote sensing models for
989 capturing intra- and inter-annual variations in daily GPP: An analysis using global
990 FLUXNET tower data. Agric. For. Meteorol. 214–215, 416–429.
991 doi:10.1016/j.agrformet.2015.09.005
992 Wang, Z., Schaaf, C.B., Lewis, P., Knyazikhin, Y., Schull, M.A., Strahler, A.H., Yao, T.,
993 Myneni, R.B., Chopping, M.J., Blair, B.J., 2011. Retrieval of canopy height using
994 moderate-resolution imaging spectroradiometer (MODIS) data. Remote Sens. Environ. 115,
995 1595–1601. doi:10.1016/j.rse.2011.02.010
996 Wehr, R., Saleska, S.R., 2015. An improved isotopic method for partitioning net ecosystem–
997 atmosphere CO2 exchange. Agric. For. Meteorol. 214–215, 515–531.
998 doi:10.1016/j.agrformet.2015.09.009
999 Welp, L.R., Randerson, J.T., Liu, H.P., 2007. The sensitivity of carbon fluxes to spring warming
1000 and summer drought depends on plant functional type in boreal forest ecosystems. Agric.
1001 For. Meteorol. 147, 172–185. doi:10.1016/j.agrformet.2007.07.010
1002 Woodcock, C.E., Strahler, A.H., Jupp, D.L.B., 1988a. The use of variograms in remote sensing. I
1003 - Scene models and simulated images. II - Real digital images. Remote Sens. Environ. 25,
1004 323–348. doi:10.1016/0034-4257(88)90108-3
1005 Woodcock, C.E., Strahler, A.H., Jupp, D.L.B., 1988b. The use of variograms in remote sensing:
1006 II. Real digital images. Remote Sens. Environ. 25, 349–379. doi:10.1016/0034-
1007 4257(88)90109-5
1008 Wu, J., Larsen, K.S., van der Linden, L., Beier, C., Pilegaard, K., Ibrom, A., 2013. Synthesis on
1009 the carbon budget and cycling in a Danish, temperate deciduous forest. Agric. For. Meteorol.
1010 181, 94–107. doi:10.1016/j.agrformet.2013.07.012
1011 Wu, Z.Y., Zhang, L., Wang, X.M., Munger, J.W., 2015. A modified micrometeorological
1012 gradient method for estimating O3 dry deposition over a forest canopy. Atmos. Chem. Phys.
1013 Discuss. 15, 779–806. doi:10.5194/acpd-15-779-2015

Xiao, X., Zhang, Q., Braswell, B.H., Urbanski, S.P., Boles, S., Wofsy, S.C., Moore, B., Ojima, D., 2004. Modeling gross primary production of temperate deciduous broadleaf forest using satellite images and climate data. Remote Sens. Environ. 91, 256–270. doi:10.1016/j.rse.2004.03.010

Xu, K., Metzger, S., Desai, A.R., 2017. Upscaling tower-observed turbulent exchange at fine spatio-temporal resolution using environmental response functions. Agric. For. Meteorol. 232, 10–22. doi:10.1016/j.agrformet.2016.07.019

Zhang, X., Friedl, M.A., Schaaf, C.L., Strahler, A.H., Hodges, J.C.F., Gao, F., Reed, B.C., Huete, A.R., 2003. Monitoring vegetation phenology using MODIS. Remote Sens. Environ. 84, 471–475. doi:http://dx.doi.org/10.1016/S0034-4257(02)00135-9